SOFIA UNIVERSITY "ST. KLIMENT OHRIDSKI"

FACULTY OF CHEMISTRY AND PHARMACY

DEPARTMENT OF APPLIED INORGANIC CHEMISTRY

Porous metals obtained by selective dissolution of alloys – suitable electrode materials in ion batteries

Evelina Yordanova Vassileva

AUTOREFERAT

of dissertation for the acquisition of educational and scientific degree

"PhD"

Scientific supervisor: ***Prof. Tony Spassov, Dr. Sci.***
Scientific advisor: ***Assist. Prof. Dr. Lyuben Mihaylov***

Scientific field: ***4.2. Chemical science***
Doctoral program: ***Solid state chemistry***

Sofia 2023

The dissertation contains 116 pages, 54 figures and 4 tables. 230 literature sources are cited.

The numbering of the figures and tables in the autoreferat corresponds to that in the dissertation.

Part of the investigations was carried out together with colleagues from the Institute of General and Inorganic Chemistry at the Bulgarian Academy of Sciences and the Department of Materials Science and Metallurgy at the University of Cambridge!

The dissertation work was supported by the European Regional Development Fund within the Operational Program „Science and Education for Smart Growth 2014 – 2020“ within the CEP project „National Center for Mechatronics and Clean Technologies“ BG05M2OP001-1.001-0008!

Introduction

The replacement of non-renewable fossil fuels with alternative sources of renewable energy is a major problem of the modern society. In order to find a solution, a lot of research is being conducted in the field of materials for efficient energy storage, especially in materials with application in lithium-ion and sodium-ion batteries. Lithium-ion batteries have already found wide application in our daily life as one of the most efficient energy storage systems for a large number of devices such as mobile phones, laptops, electric vehicles, etc. Due to their ability to store large amounts of energy, their consumption is constantly increasing, which requires the development and optimization of new electrode materials.

The advantages of porous materials when used as electrodes in ion batteries comes from their large specific surface area with many active centers, the ease passage of the electrolyte and the diffusion of ions through the porous structure. Another advantage is that it is not necessary to use binder agents when preparing the electrodes. One of the main and commonly used approaches to obtain porous structures is based on the selective dissolution of multicomponent metal alloys. Thus, depending on the initial composition and properties of the material, structures with different pore size and shape can be obtained, which allows their modeling for specific applications.

Goals and tasks

The present dissertation work has several main goals. The first is the preparation of two-component (Zn-Sn) and three-component (Zn-Sn-Bi и Cu-Ag-Al) alloys under different crystallization conditions from a melt. The next goal is the electrochemical selective dissolution of the less noble metal from the alloys and obtaining porous structures. The application of some of the porous materials for electrochemical energy storage was also an important goal of the dissertation research.

The specific research tasks can be formulated as:

- ✓ Obtaining a series of alloys applying two different approaches – through rapid quenching from a melt and via standard casting on a smooth ceramic surface;
- ✓ Optimizing the experimental conditions of the electrochemical dissolution (type and concentration of electrolyte, electrode potential, time) in order to obtain porous structures;
- ✓ Investigating the changes in the morphology and microstructure of the materials before and after selective dissolution;
- ✓ Studying the potential application of the obtained porous materials as electrodes in lithium- and sodium-ion batteries.

Results and discussion

Zn-Sn and Zn-Sn-Bi based alloys

A series of microcrystalline Zn-Sn and Zn-Sn-Bi alloys obtained by two different methods were studied – synthesized by normal cooling (casting on a smooth ceramic surface) with thickness of about 70 μm and by rapid quenching, which was accomplished by induction melting of the pure metals in a quartz tube under inert atmosphere and casting onto rotating copper disk. The alloys were produced at rotation disk speed of 2500 rpm with about 50 μm thickness and 1 cm width. The alloy obtained by normal cooling is with composition $Zn_{70}Sn_{30.}$ The composition of the alloys synthesized by rapid quenching are $Zn_{70}Sn_{30,}$ $Zn_{70}Sn_{25}Bi_{5,}$ $Zn_{70}Sn_{15}Bi_{15}$ and $Zn_{70}Sn_{5}Bi_{25.}$ The microstructure of the initial alloys, as well as after the various electrochemical experiments, was examined by X-ray diffraction with diffractometers Bruker D8 Advance with CuKα radiation and Seifert XRD with CuKα radiation, and also with a transmission electron microscope - JEOL JEM 2100, 200 kV. The chemical composition of the alloys before and after selective dissolution was confirmed by energy-dispersive spectroscopy - EDX/JEOL JEM 2100. Differential scanning calorimeter was used to study the thermal stability of the alloys – TA DSC250. The morphology of the selectively dissolved samples was studied with a scanning electron microscope - SEM JEOL 5510. All electrochemical experiments were performed in a three-electrode cell with potentiostat-galvanostats PARSTAT 2273 and Autolab PGSTAT 302N. The electrochemical charge-discharge experiments were carried out using Swagelok two-electrode cell, where metallic lithium or sodium was used as anode, porous alloy as a cathode, 1 M $LiPF_6$ in ethylene carbonate (EC) and dimethyl carbonate (DMC), or 1 M $NaPF_6$ in polypropylene carbonate (PPC) as electrolytes, and Whatman separator. The sodium and lithium electrodes are in the form of discs with a diameter of 10 mm. The data were recorded on an Arbin BT2000 system.

1. Eutectic $Zn_{70}Sn_{30}$ alloy

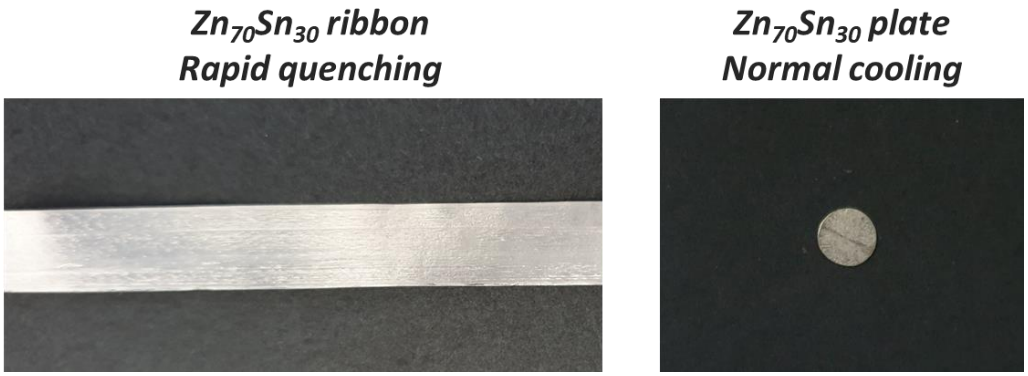

Fig. 9. Picture of the two types of electrodes obtained under different cooling conditions.

1.1. Morphology and microstructure

X-ray analysis

X-ray diffraction analysis of the both $Zn_{70}Sn_{30}$ alloys was carried out in order to confirm the effect of the rapid quenching, which we assume that leads to the formation of smaller crystallites, defects or different phases, Fig. 10. The results show a small difference in the microstructure of the two alloys. The Sn peaks are slightly shifted due to the formation of Sn(Zn) solid solution. The broadening of the diffraction peaks in the rapidly quenched alloy is an indicator of the smaller size of Zn and Sn crystallites. Additionally, (002) crystallographic texture of Zn crystallites is observed only in the conventionally cast alloy.

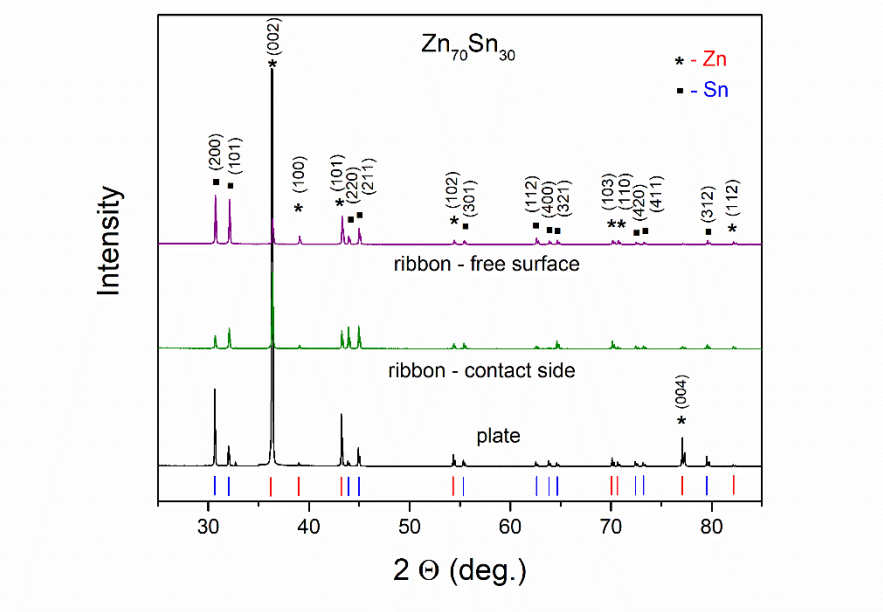

Fig. 10. XRD of the as-cast $Zn_{70}Sn_{30}$ alloys.

Transmission electron microscopy

The samples for TEM were attached in a three-component epoxy resin and cut with an UltraMicrotome (Leica EM UC7) with ~ 20 nm slice thickness.

Transmission electron microscopy was used to confirm the two-phase microstructure of the two $Zn_{70}Sn_{30}$ alloys, as well as to characterize the crystallite morphology, Fig. 11. Distinct difference in the crystallite size of the conventionally and rapidly quenched alloys can be observed from the electron micrographs. Rapid quenching results in crystallites size reduction, decreasing from about 300 nm for the slow cast to about 100 nm for the rapidly quenched alloys. It should be noted that this significant difference was not detected by X-ray diffraction due to the relatively large size of the crystal grains. In the alloy crystallized more slowly, two areas with different morphology of the crystallites are observed. One has relatively equiaxed crystallites, and the other domain colonies of polycrystalline Zn with elongated shape are detected. This can also be clearly seen from the STEM images in Fig. 12.

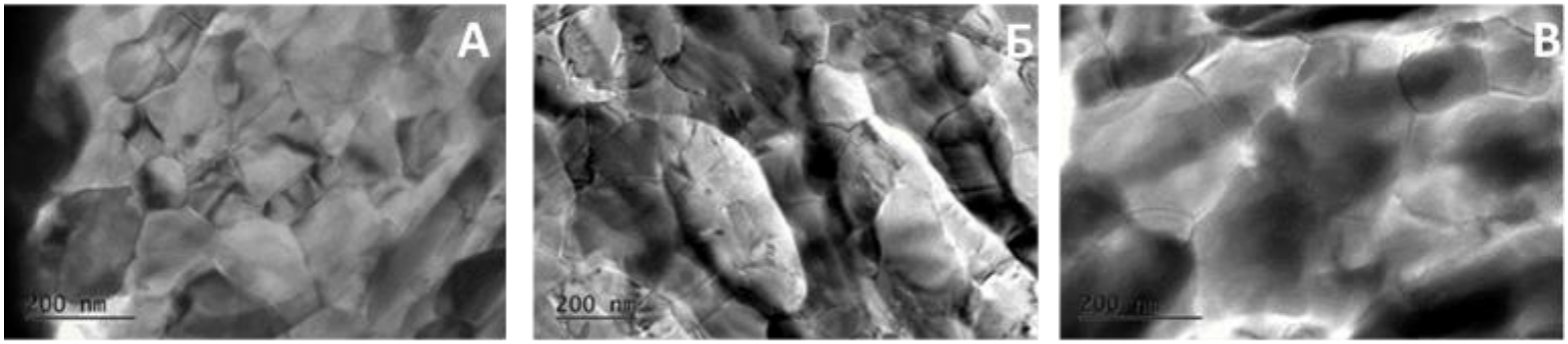

Fig. 11. TEM of as-cast $Zn_{70}Sn_{30}$ alloys: (А,Б) conventionally cast and (В) rapidly quenched.

Energy-dispersive spectroscopy

Additional microstructural information was obtained from the EDS analysis – in conventionally cast alloy, there are crystals of nearly pure Zn, which build a 3-D network of the Zn phase, Fig. 12. Futhermore, the Sn crystals in the rapidly quenched alloy show higher content of Zn (4-5 at. %), compared to the equilibrium Zn concentration in the Sn(Zn) solid solution - < 1 at. %, Fig. 13. The elements composition in the plate are Zn – 69.40 at. % and Sn – 30.60 at. %, and in the ribbon : Zn – 65.84 at. % and Sn – 34.16 at. %.

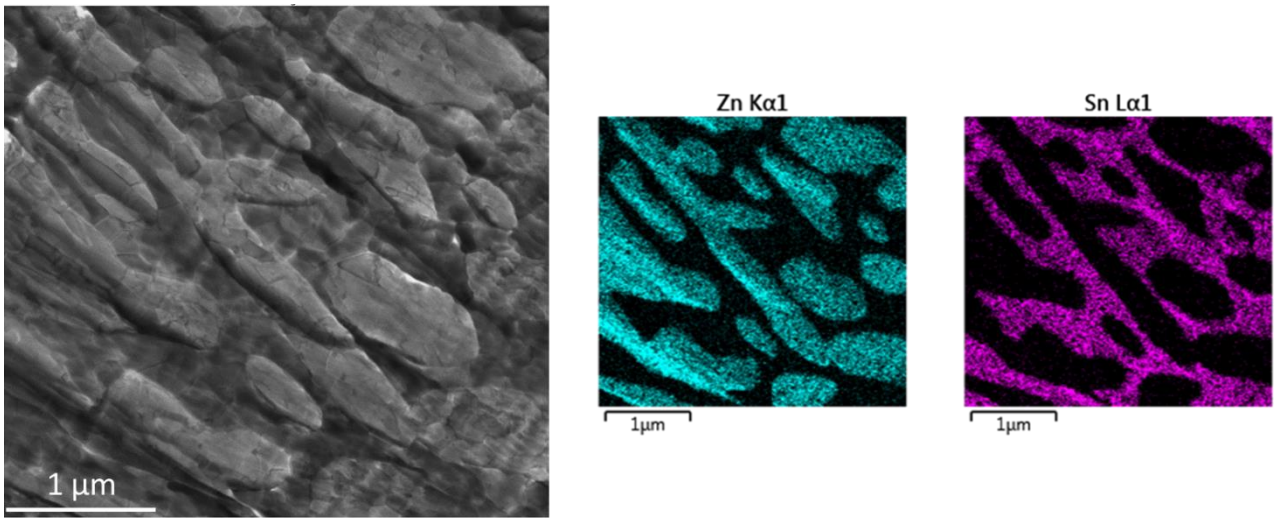

Fig. 12. STEM and EDS of conventionally cast $Zn_{70}Sn_{30}$ alloy.

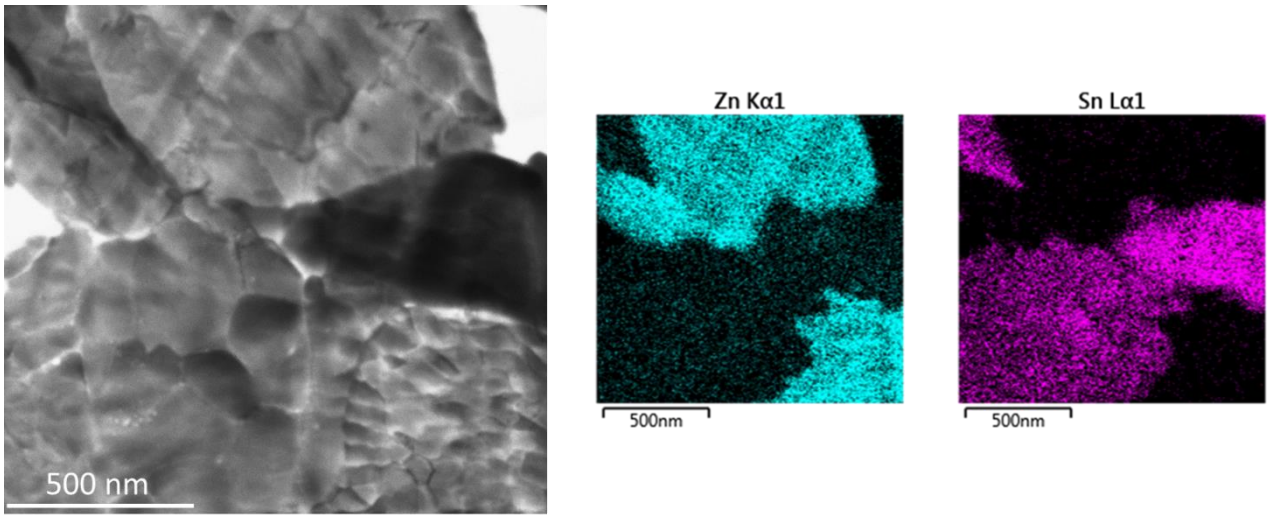

Fig. 13. STEM and EDS of rapidly quenched $Zn_{70}Sn_{30}$ alloy.

1.2. Formation of the porous structure by selective electrochemical dissolution of the alloys

The next goal of our study was to obtain porous structures by selective electrochemical dissolution of the synthesized alloys. It is important to note that this type of low-temperature alloys has not undergone selective dissolution up to date. The electrode potential and the electrolyte are selected to provide the selective dissolution of Zn and thus to increase the surface area of the Sn phases. It was found that the longer selective dissolution time results in poor mechanical stability of the porous electrodes.

In order to select the optimal conditions for the electrochemical selective dissolution, potentiodynamic polarization experiments were performed at a scan rate of 10 mV/s, Fig. 14. The polarization curves of the alloy show a difference in the corrosion potentials of the two alloys obtained with different cooling rates. The corrosion stability of the rapidly quenched alloy in 0.1 M $HClO_4$ is slightly better compared to the slowly cooled $Zn_{70}Sn_{30}$. There is no passivation region for both alloys.

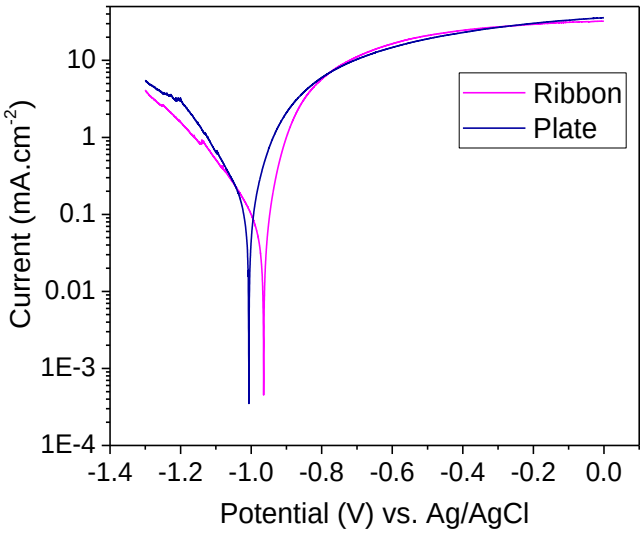

Fig. 14. Potentiodynamic polarization curves of $Zn_{70}Sn_{30}$ alloys obtained at different cooling rates in 0.1 M $HClO_4$ water solution.

The potential for the selective electrochemical dissolution for all of the studied alloys was –100 mV (vs. Ag/AgCl) in 0.1 M $HClO_4$ electrolyte for 1800 s.

At the beginning, the current increases significantly for a very short time for both alloys and then slows down and gradually decreases. The corrosion current density in the ribbon reaches a higher value, but in the middle of the process there is decrease and the current value at the end of the process is lower. In the conventionally cooled alloy, the current decreases at a constant rate without rapid changes.

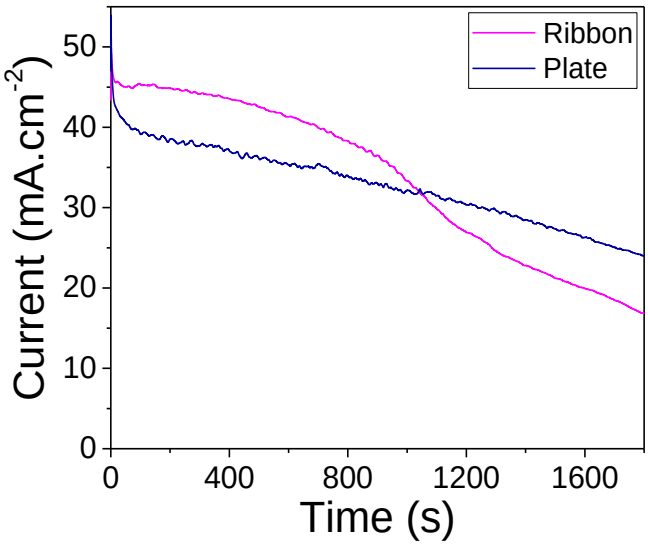

Fig. 15. Potentiostatic curves of $Zn_{70}Sn_{30}$ alloys obtained at different cooling rates in 0.1 M $HClO_4$ at –100 mV (vs. Ag/AgCl).

XRD of the porous materials was carried out to study the microstructural changes after the selective dissolution. Almost complete dissolution of Zn from both alloys was confirmed, Fig. 16. The diffraction peaks corresponds to the pure Sn phase, proving that the dissolution affects only Zn crystallites, as the remaining Sn crystallites form inter-connected ligaments structure. It is also important to note that whereas in the initial $Zn_{70}Sn_{30}$ alloy, the Sn peak positions are slightly shifted to higher angles due to the formation of Sn(Zn) solid solution, after dealloying this shift vanishes, explained by the Zn dissolution from the Sn(Zn) crystallites as well.

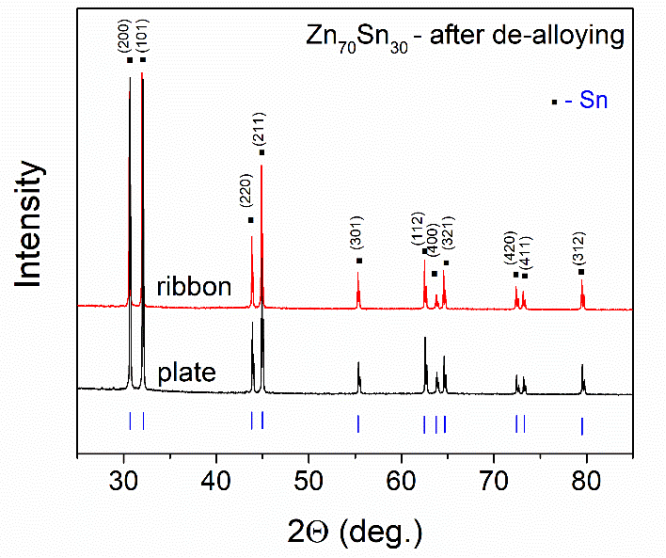

Fig. 16. XRD of $Zn_{70}Sn_{30}$ alloys after selective electrochemical dissolution.

The morphology of the alloys after potentiostatic experiments was examined with scanning electron microscope. SEM images reveals a three-dimensional inter-penetrated porous structure of both alloys, Fig. 17. and Fig. 18. However, there is a clear difference in the ligaments and pore size in the two alloys obtained under different conditions.

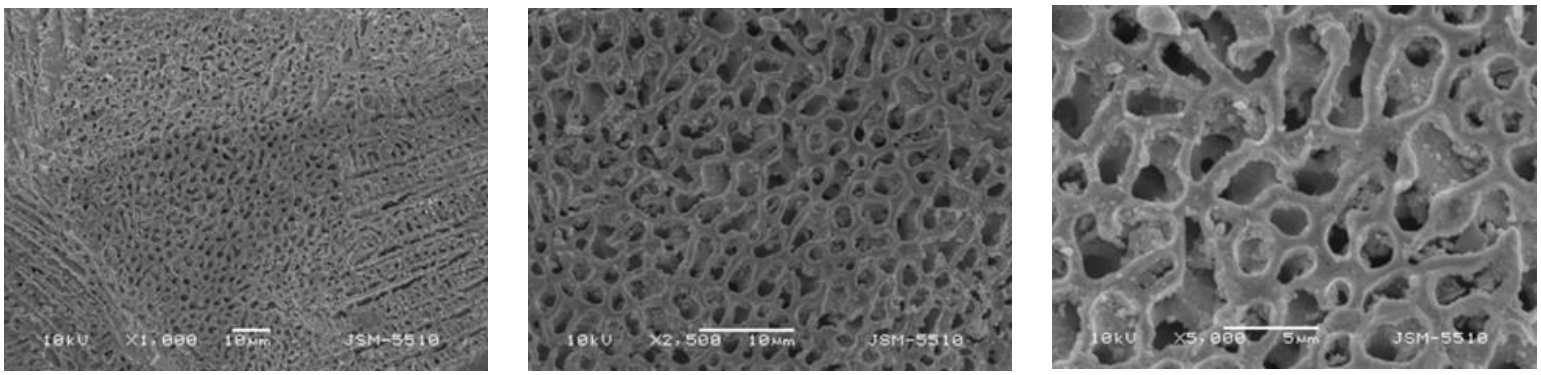

Fig. 17. SEM micrographs of the selectively dissolved $Zn_{70}Sn_{30}$ plate.

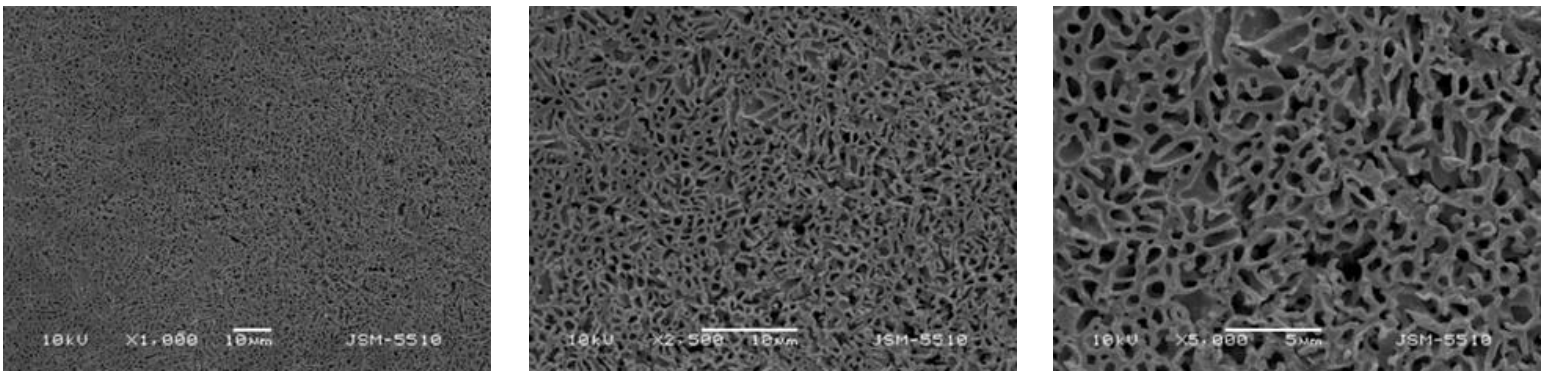

Fig. 18. SEM micrographs of the selectively dissolved $Zn_{70}Sn_{30}$ ribbon.

Fig. 19 shows the pore size distribution of the alloys prepared by the two methods, where around 300-400 pores were measured. The smaller crystallites of the ribbon formed during the rapid quenching result in smaller pores – average pore size 500 nm, compared to the conventionally cast alloy with the same composition, which forms much larger pores – average pore size 1500 nm.

The surface area, S_{BET} of the melt-spun $Zn_{70}Sn_{30}$ was determined to be larger - 2 m^2 g^{-1} than that of the conventionally cast plate - 0.5 m^2 g^{-1}. The difference can be attributed to the finer microstructure of the rapidly quenched material.

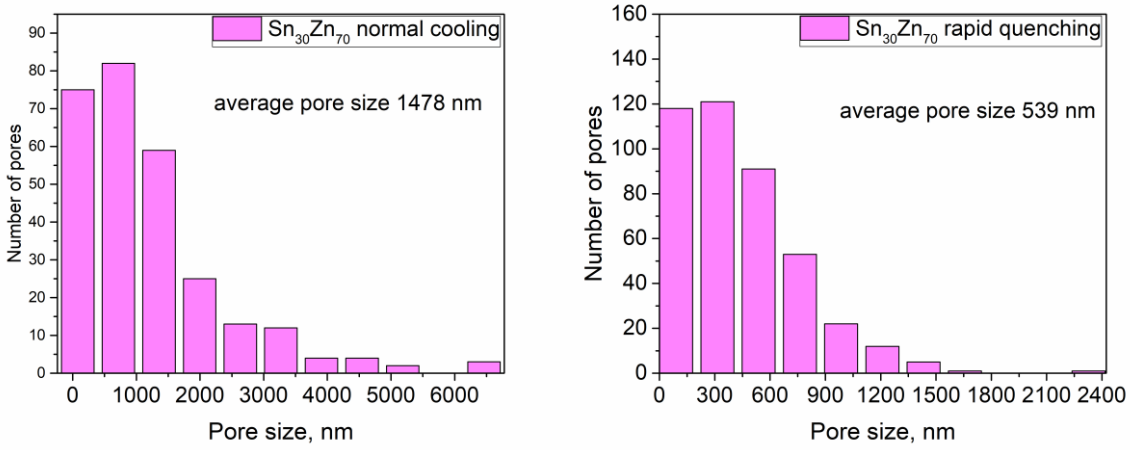

Fig. 19. Pore size distribution of the dealloyed $Zn_{70}Sn_{30}$ alloys.

Additional information about the size of the pores and the ligaments, as well as their distribution in the sample volume gives the cross-sectional SEM of the porous structures, Fig. 20. A homogeneous porosity along the whole volume of both alloys is clearly observed. Some difference in the ligaments morphology of the alloys obtained with different cooling rates could however be seen: the slow cooled alloy shows rod-like ligaments shape, perpendicular to the sample plane, whereas in the rapidly quenched alloy the ligamets exhibit mostly a particle-like shape. The observed rod-like ligaments morphology in the conventionally cast alloy can be explained by the preferred crystallites growth in a direction perpendicular to the sample plane, following the temperature gradient through the sample thickness occurring during the slow cooling. In contrast, in the melt-spun alloy, the crystallization proceeds rapidly throughout the volume of the ribbon forming particle-shaped ligaments.

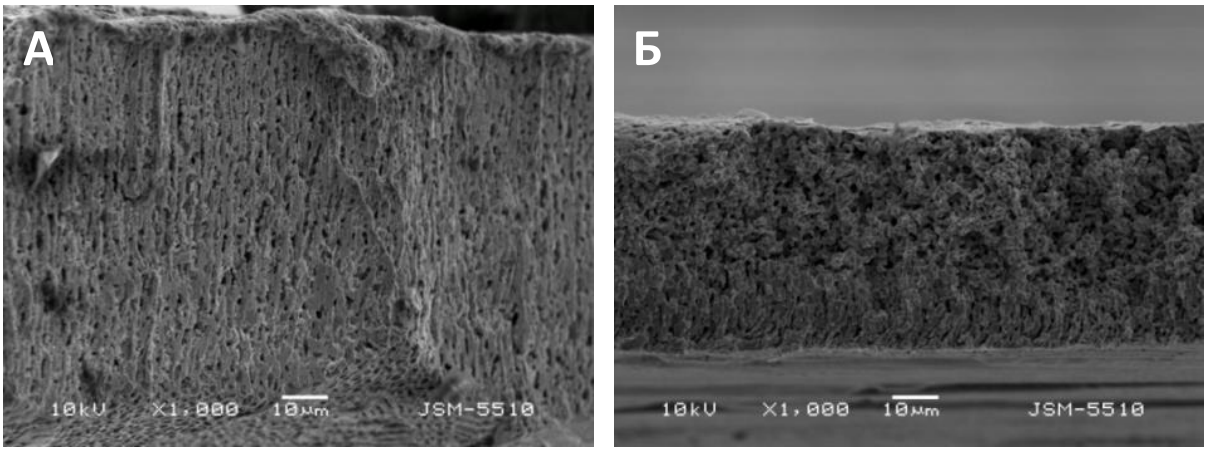

Fig. 20. SEM cross section micrographs of de-alloyed plate (А) and ribbon (Б).

1.3. Electrochemical capacity of the synthesized porous structures as electrodes in ion batteries

Due to the superior combination of desired properties like mechanical stability, appropriate thickness, smaller pores and homogeneous pore distribution across the ribbon surface, only the rapidly quenched ribbon has been investigated as electrode in Li^+/Na^+ ion cells. From the charge/discharge curves it can be seen that after the first discharge, the specific capacity in Li ion cell is higher than that in the Na ion cell: 440 mAh/g in Li and 205 mAh/g in Na cell, Fig 21. This result is in accordance with the different theoretical capacity of Sn during lithiation and sodiation, 994 mAh/g и 847 mAh/g, respectively. It is worth mentioning that the experimental specific capacities of the porous structures are obtained without any binders and conductive additives, which is typical for tin-based electrode fabrication in Li- and Na-ion batteries.

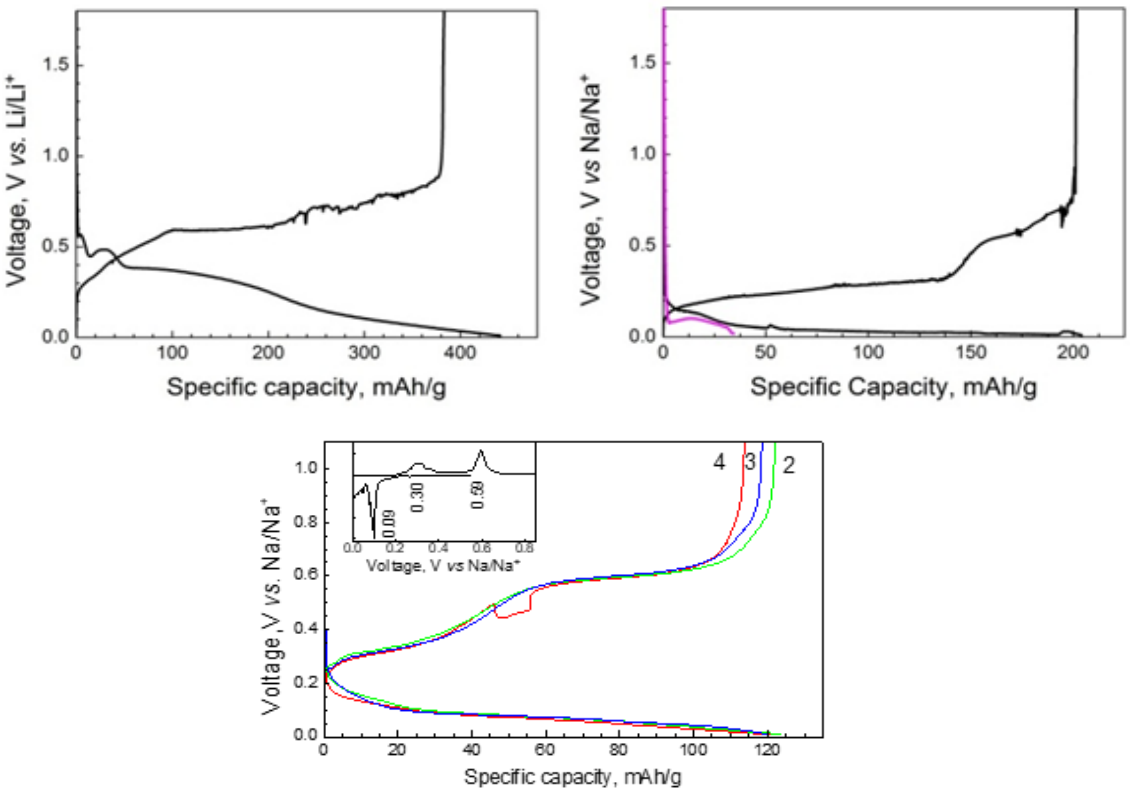

Fig. 21. First charge/discharge curves of the porous ribbon in Li- and Na-cells. The first sodiation curve of the conventionally cast alloy in also given (in magenta colour). The charge/discharge curves at 2nd, 3rd and 4th cycles for $Zn_{70}Sn_{30}$ ribbon.

After the reverse process of charging, nearly the same capacity is delivered, especially in the Na-ion cell: 382 mAh/g vs. 200 mAh/g. The charge/discharge curve profiles indicates that the lithiation process proceeds at slopping redox plateau at 0.37V/0.60V vs. Li/Li^+, while the sodiation takes place in more structured way by developing discharge and charge plateaus at 0.14 – 0.04 V and 0.28 – 0.57 V vs. Na/Na^+. The lowest potential of interaction of the ribbon alloy with Na^+ is 0.09 V, just above that of the metallic Na deposition, Fig. 21 (inset). Because the Na plating proceeds more easily at low temperatures and high charging rates, all electrochemical experiments are performed at room temperature and a rate of C/20.

In general, the observed curve profiles in both Li- and Na-ion cells are similar to that reported previously. This means that the porous structures are able to interact both with Li^+ and Na^+ by alloying. Furthermore, the stability of the capacity during cycling is different. Further cycles provoke a quick drop of the capacity in Li-ion cell, while in Na-ion cell, there is relatively good capacity retention: the discharge capacity decreases

from 205 to around 120-130 mAh/g and remains constant during cycling. The cycling stability is related with mechanical stability of the porous structures.

The effect of the porous structure is demonstrated by the interaction of Na^+ with rapidly quenched alloy and conventionally cast alloy with the same composition. As can be seen from Fig. 21 in magenta colour, the specific capacity of the plate reaches only 35-40 mAh/g, which is significantly lower (more than 5 times) than that of the ribbon alloy - 205 mAh/g. The different behaviour of plate and ribbon alloys can be related with their surfaces and microstructure: the larger surface area and microstructure including defects and higher density of intercrystalline boundaries due to the smaller crystallites, are favorable for achieving enhanced sodium storage.

During electrochemical lithiation, metallic Sn can react with Li and form various intermetallic compounds – Li_xSn ($0 < x < 4.4$). The specific theoretical capacity of the lithium-rich phase $Li_{4.4}Sn$ is 994 mAh/g, and the occurring reversible reaction is [218,219]:

$$Sn + xLi^+ + xe^- \leftrightarrow Li_xSn\ (0 < x < 4.4).$$

If we also consider SnO_2, which has a specific theoretical capacity of the bulk SnO_2 of 780 mAh/g, and 1484 mAh/g of the nanosized SnO_2, the chemical reactions reactions with lithium electrodes proceed in two steps [218,219]:

$$SnO_2 + 4Li^+ + 4e^- \rightarrow Sn + 2Li_2O$$

$$Sn + xLi^+ + xe^- \leftrightarrow Li_xSn\ (0 < x < 4.4).$$

Sodium also forms phases with tin, but it is found that during sodiation only the equilibrium cubic $Na_{15}Sn_4$ phase is formed. The theoretical specific capacity of $Na_{15}Sn_4$ is 847 mAh/g, and that of SnO_2, which also interacts with Na is 1378 mAh/g. In this case, the reversible reaction takes place first: $SnO_2 + 4Na^+ + 4e^- \leftrightarrow Sn + Na_2O$, followed by the reversible alloying [218,220].

2. Zn-Sn-Bi alloys

2.1. Morphology and microstructure

X-ray analysis

The rapidly quenched ribbons with compositions $Zn_{70}Sn_5Bi_{25}$, $Zn_{70}Sn_{15}Bi_{15}$ and $Zn_{70}Sn_{25}Bi_5$ show a well defined crystalline structure, Fig. 22. The diffraction peaks of the three metals composing the as-spun materials are well distinguished with some displacements of some peaks' maximums due to the formation of solid solutions. This effect, obtained as a result of the rapid quenching, is most clearly observed for the tin-based solid solutions, Sn(Zn) and Sn(Bi).

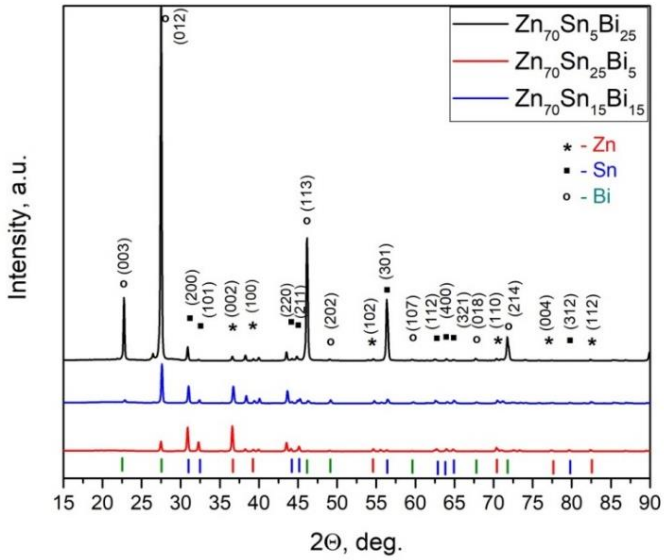

Fig. 22. XRD patterns of the as-cast $Zn_{70}Sn_5Bi_{25}$, $Zn_{70}Sn_{15}Bi_{15}$ and $Zn_{70}Sn_{25}Bi_5$ alloys.

Thermal stability

In order to evaluate the effect of the microstructure of the initial alloys on the porous structure after de-alloying, it is important to obtain certain quantitative information for the alloys phase composition, including ternary eutectics and other crystalline phases. The thermal curves of the initial as-cast alloys clearly show the melting of the ternary

eutectics first, followed by the melting peaks of the other crystalline phases, Fig 23. The melting point of the ternary eutectic is about 130 ℃, which is about 70 ℃ lower than that of the binary Zn-Sn eutectic. After the melting of the ternary eutectic in $Zn_{70}Sn_{15}Bi_{15}$, melting of practically pure zinc follows. The melting sequence of the crystalline phases is in accordance with the phase diagrams and information available in the literature [221]. In the alloy $Zn_{70}Sn_{25}Bi_5$, after the eutectic, the tin-rich phase is melted and finally the zinc. In $Zn_{70}Sn_5Bi_{25}$, the eutectic melting is followed by melting of the bismuth-rich crystals and finally almost pure zinc melts.

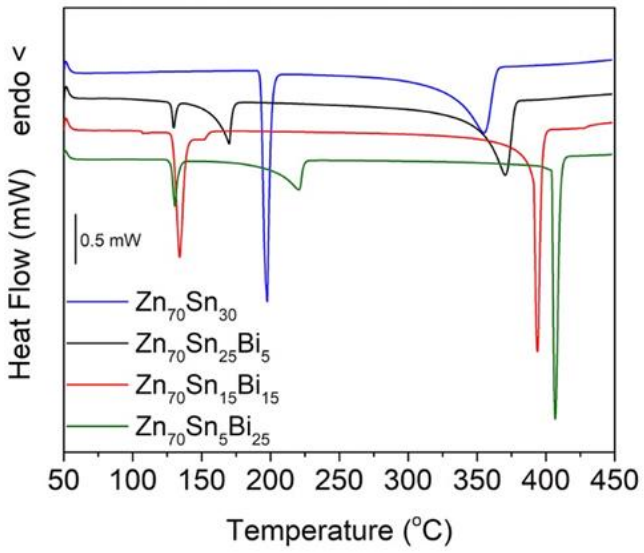

Fig. 23. DSC curves of the melt-spun alloy ribbons.

From the melting enthalpies of different crystalline phases present in the alloys, their quantitative ratio could be determined. Thus, maximum amount of ternary eutectic (~ 40 wt.%) is measured in $Zn_{70}Sn_{15}Bi_{15}$, while in $Zn_{70}Sn_{25}Bi_5$ alloys it is less than 10 %. The alloy with the highest amount of bismuth is also characterized by the highest melting temperature value of 420 ℃.

Transmission electron microscopy

TEM analysis allowed us a more detailed characterization of the $Zn_{70}Sn_5Bi_{25}$, $Zn_{70}Sn_{15}Bi_{15}$ and $Zn_{70}Sn_{25}Bi_5$ ribbons obtained by rapid quenching. In all alloys, there are areas with the presence of eutectic colonies, more pronounced in $Zn_{70}Sn_{15}Bi_{15}$, Fig. 25. Elongated zones composed of more or less equiaxed Zn, Sn and Bi crystallites alternate in the microstructure of the ribbons. Outside the eutectic colonies, the crystallites of all three alloys also reveal a regular shape. The average crystallite size of less than 200 nm was determined for all compositions. As expected, while for the composition $Zn_{70}Sn_{25}Bi_5$ predominate Zn and Sn crystallites, in $Zn_{70}Sn_5Bi_{25}$ prevail Zn and Bi crystallites, and for $Zn_{70}Sn_{15}Bi_{15}$ there is uniform and equal amount of Sn and Bi crystallites and significantly higher amount of Zn phase. It should be noted that the crystallites of alloys obtained by rapid quenching are significantly smaller than those of similar alloys cast under standart low cooling rate conditions, which was also proved recently in our study of the $Zn_{70}Sn_{30}$ alloy.

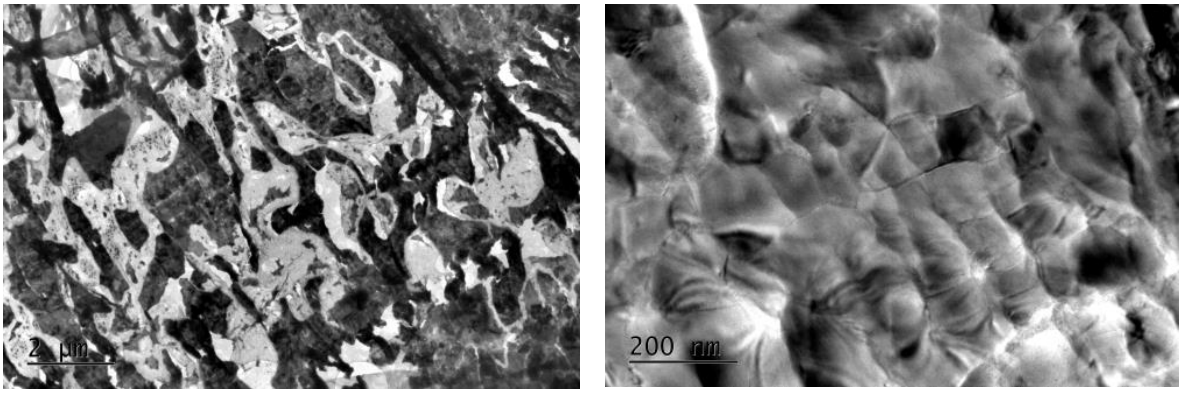

Fig. 24. TEM micrographs of $Zn_{70}Sn_{25}Bi_5$.

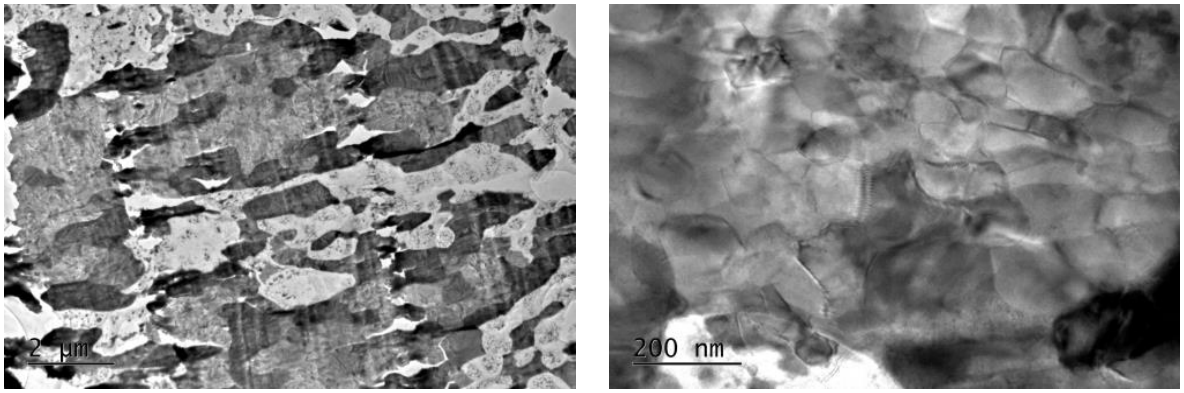

Fig. 25. TEM micrographs of $Zn_{70}Sn_{15}Bi_{15}$.

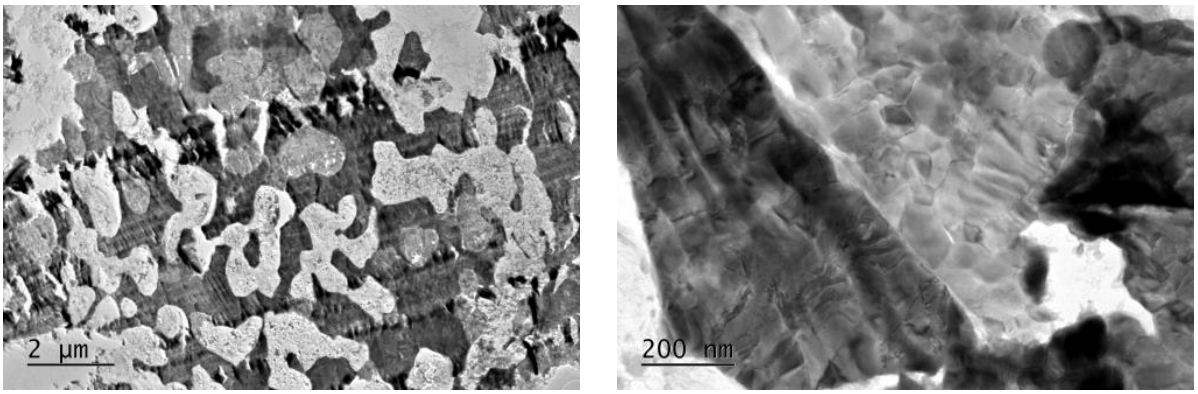

Fig. 26. TEM micrographs of $Zn_{70}Sn_5Bi_{25}$.

Energy-dispersive spectroscopy

Elemental analysis revealed that the composition of the alloys after casting corresponds to the nominal one. The EDS analysis also confirmed the presence of eutectic colonies of alternating crystalline regions of the three metals. This is most clearly observed in the composition $Zn_{70}Sn_{15}Bi_{15}$, Fig. 27. The Bi and Zn regions are mostly in contact, so that they can form a three-dimensional porous structure upon subsequent selective dissolution of the Zn phase. In addition, it provides information about the existing solid solutions, evidently extended as a result of the rapid quenching.

As expected, the most pronounced are the solid solutions based on Sn, as both solutes about 5 at.%. The content of the elements is summarized in Table 2.

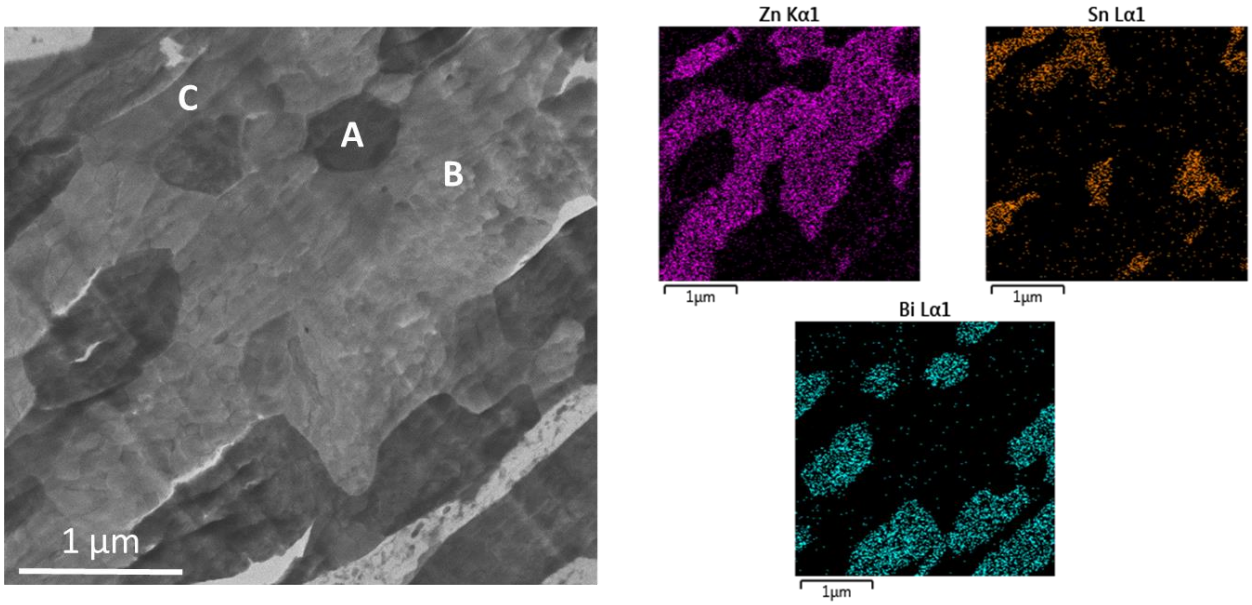

Fig. 27. STEM and EDS of $Zn_{70}Sn_{15}Bi_{15}$ ribbon.

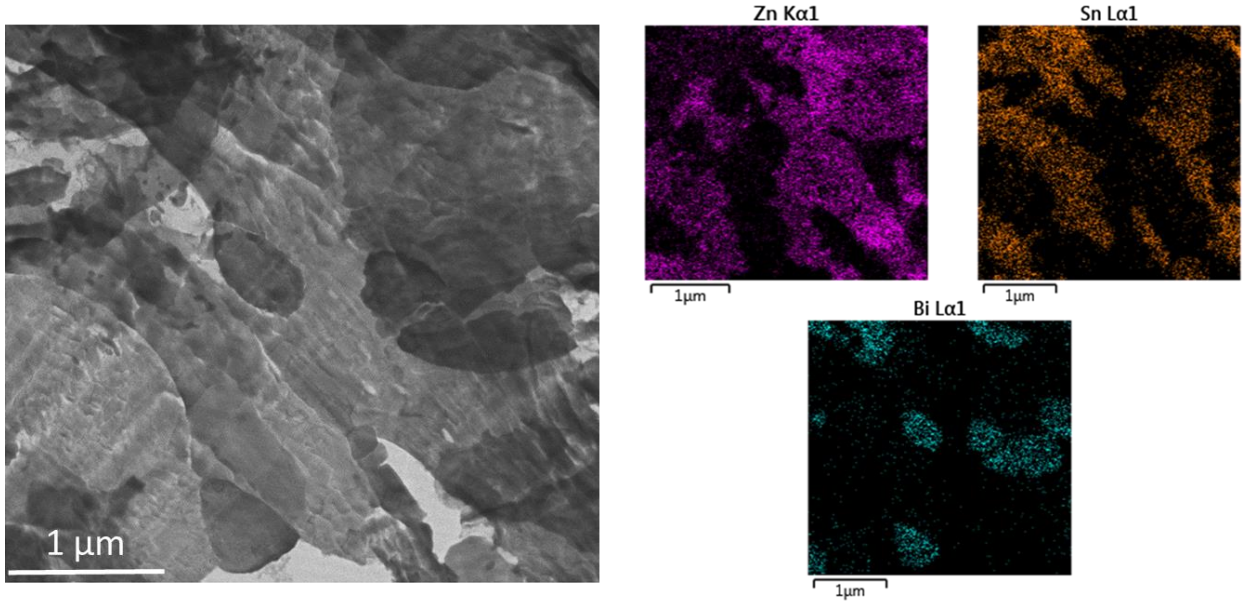

Fig. 28. STEM and EDS of $Zn_{70}Sn_{25}Bi_{5}$ ribbon.

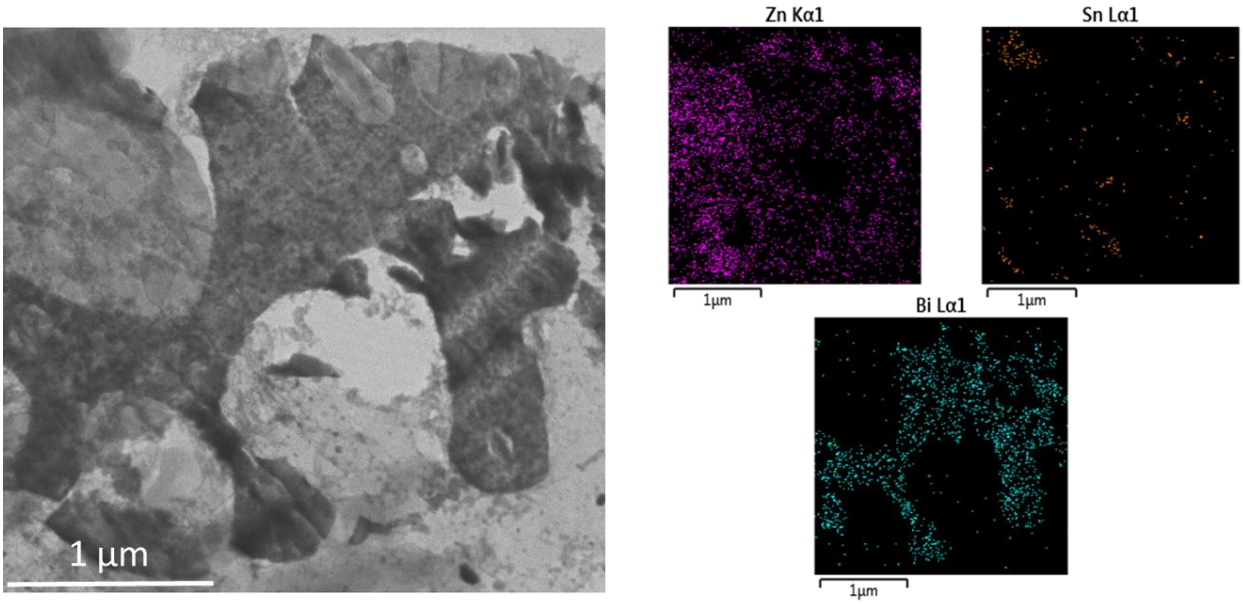

Fig. 29. STEM and EDS of $Zn_{70}Sn_5Bi_{25}$ ribbon.

	Zn, at.%	**Sn, at.%**	**Bi, at.%**
$Zn_{70}Sn_{15}Bi_{15}$	69.54	16.02	15.45
$Zn_{70}Sn_{15}Bi_{15}$ - A	~ 6	~ 1	~ 93
$Zn_{70}Sn_{15}Bi_{15}$ - B	~ 92	~ 3	~ 5
$Zn_{70}Sn_{15}Bi_{15}$ - C	~ 5	~ 90	~ 5
$Zn_{70}Sn_{25}Bi_5$	69.05	26.04	4.91
$Zn_{70}Sn_5Bi_{25}$	68.51	4.53	26.96

Table 2. Distribution of the elements from STEM-EDS for the three alloys.

2.2. Formation of the porous structure by selective electrochemical dissolution of the ternary alloys

Similar to the investigated $Zn_{70}Sn_{30}$ alloys, in this case also the next goal is to obtain porous structures by selective electrochemical dissolution. The potential and electrolyte are chosen so that the selective dissolution of zinc occurs and the active surface area of Sn and Bi phases increases. It was found that a longer dissolution time leads to poor mechanical stability of the resulted porous electrodes.

The potentiodynamic polarization experiments for the $Zn_{70}Sn_5Bi_{25}$, $Zn_{70}Sn_{15}Bi_{15}$ and $Zn_{70}Sn_{25}Bi_5$ alloys were performed at a scan rate of 10 mV/s, Fig. 30. The polarization curves show no obvious difference in the corrosion potentials of the three alloys, despite the difference in chemical composition. There is also no significant difference in the curves and no passivation region is observed for any of the studied alloys.

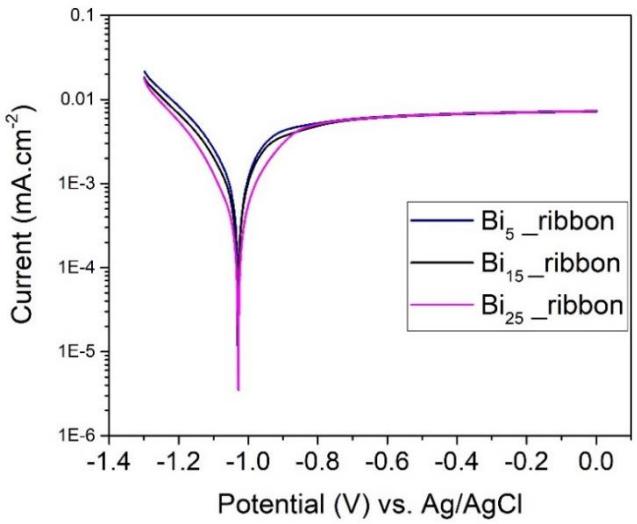

Fig. 30. Potentiodynamic polarization curves of $Zn_{70}Sn_5Bi_{25}$, $Zn_{70}Sn_{15}Bi_{15}$ and $Zn_{70}Sn_{25}Bi_5$ ribbons in 0.1 M $HClO_4$ water solution.

The chosen potential for selective electrochemical dissolution for all alloys is –100 mV (vs. Ag/AgCl) in 0.1 M $HClO_4$ electrolyte for 1000 s.

From the potentiostatic curves obtained at a potential corresponding to the selective dissolution of Zn, it is noteworthy that the process for all three alloys starts at almost the same corrosion current, Fig. 31. The bismuth-richest alloy reaches the lowest current after 1000 s, which is an indicator for faster selective dissolution. If Zn is completely dissolved, the resulting porous structure becomes brittle and fragile, especially for the $Zn_{70}Sn_5Bi_{25}$, which is also the reason the complete dissolution of zinc is not finished (the current value to reach 0 $A.cm^{-2}$).

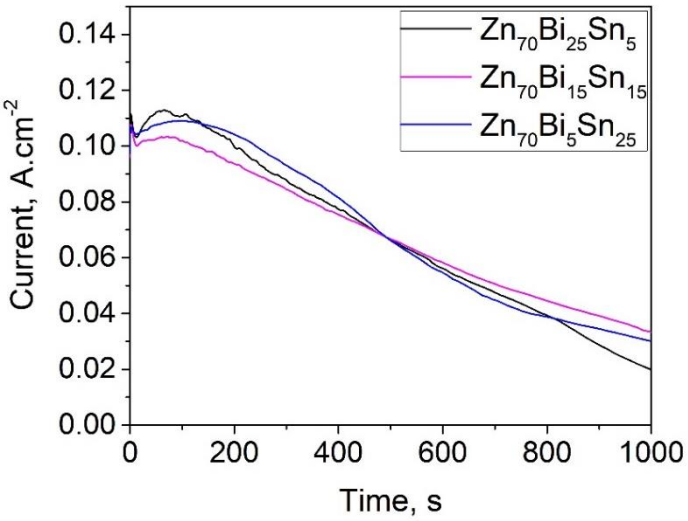

Fig. 31. Potentiostatic curves of $Zn_{70}Sn_5Bi_{25}$, $Zn_{70}Sn_{15}Bi_{15}$ and $Zn_{70}Sn_{25}Bi_5$ alloys in 0.1 M $HClO_4$ at – 100 mV vs. Ag/AgCl.

The porous structure is characterized by some differences for the alloys with different compositions, Fig. 32, Fig. 33, Fig. 34. While the alloys with 5 and 15 at.% Bi are characterized by a worm-like morphology of the ligaments formed after dissolution, in the case of the bismuth-richest alloy the morphology of the porous material is significantly different, resembling a microstructure similar to that of human bones. Although, in general the shape and the size of the pores for all alloys corresponds to those of the Zn phase before de-alloying, some differences in the pores and ligament size of the different composition also exist. In the alloy with initial composition $Zn_{70}Sn_{15}Bi_{15}$ both the pore size (~ 200 nm) and the thickness of the ligaments (~ 600 nm) are larger than those in the morphologically similar $Zn_{70}Sn_{25}Bi_5$ (~ 300 nm ligament

size and smaller pores). Unlike the first two alloys, the pores of the bismuth-richest alloy are much larger (about 1 μm).

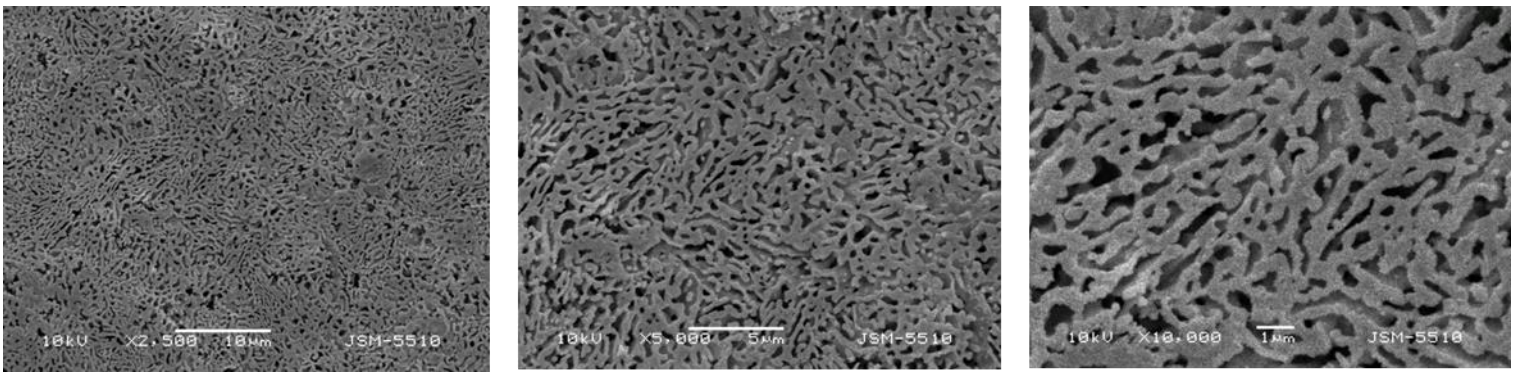

Fig. 32. SEM micrographs of the selectively dissolved $Zn_{70}Sn_{25}Bi_5$ alloy.

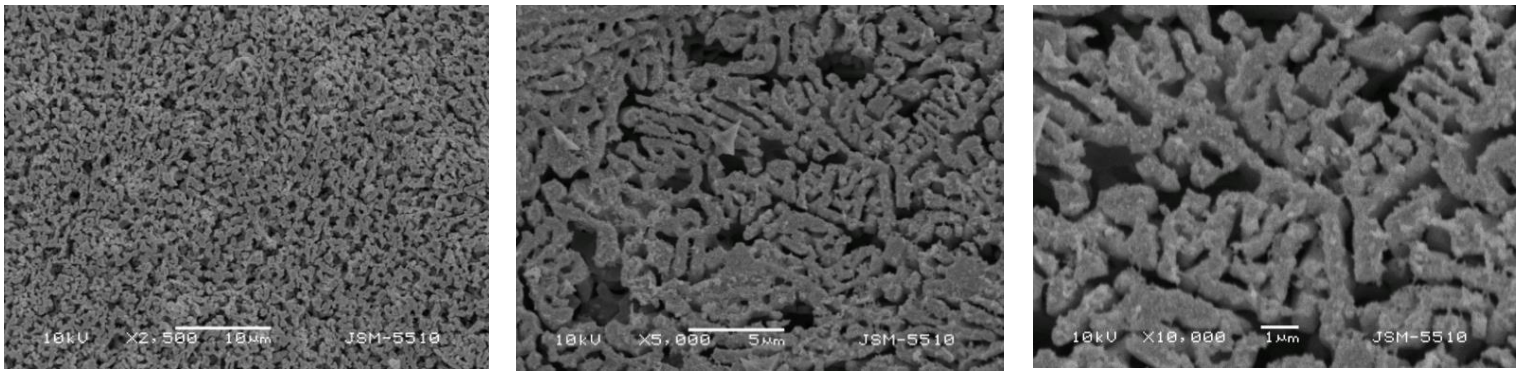

Fig. 33. SEM micrographs of the selectively dissolved $Zn_{70}Sn_{15}Bi_{15}$ alloy.

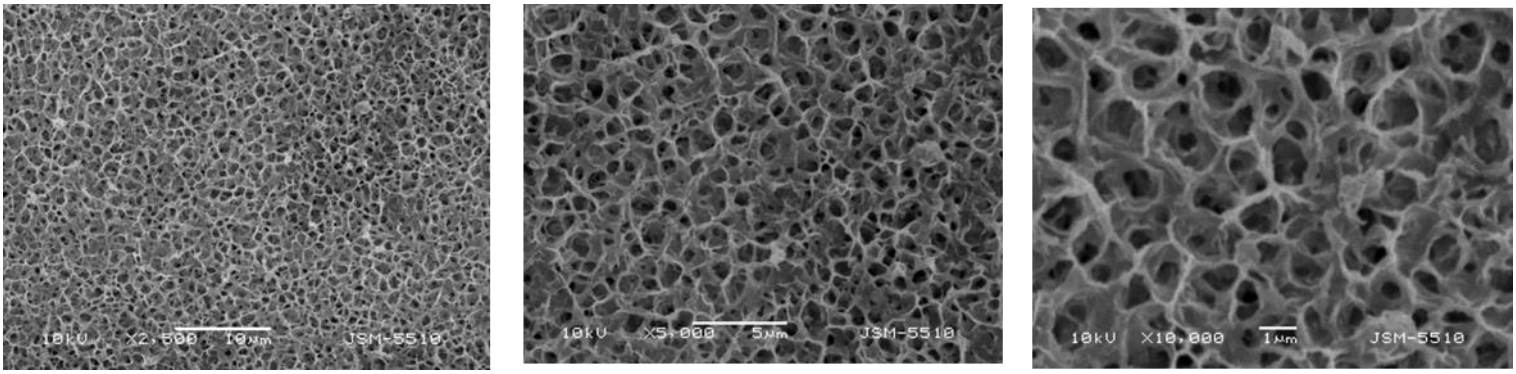

Fig. 34. SEM micrographs of the selectively dissolved $Zn_{70}Sn_5Bi_{25}$ alloy.

For all three compositions the cross-sectional SEM analysis of the porous alloys confirmed the uniform porosity affecting the entire thickness of the ribbons, Fig. 35. The already mentioned morphological differences due to the initial alloys' compositions, are confirmed. The observed differences in the morphology and pore size between the three alloys obviously have to be attributed to the different initial composition of the alloys and therefore different phase composition. The diffusion mobility of the atoms that form the porous alloys are also different – there exist significant differences in the diffusion coefficients of Sn and Bi in similar alloys [222,223].

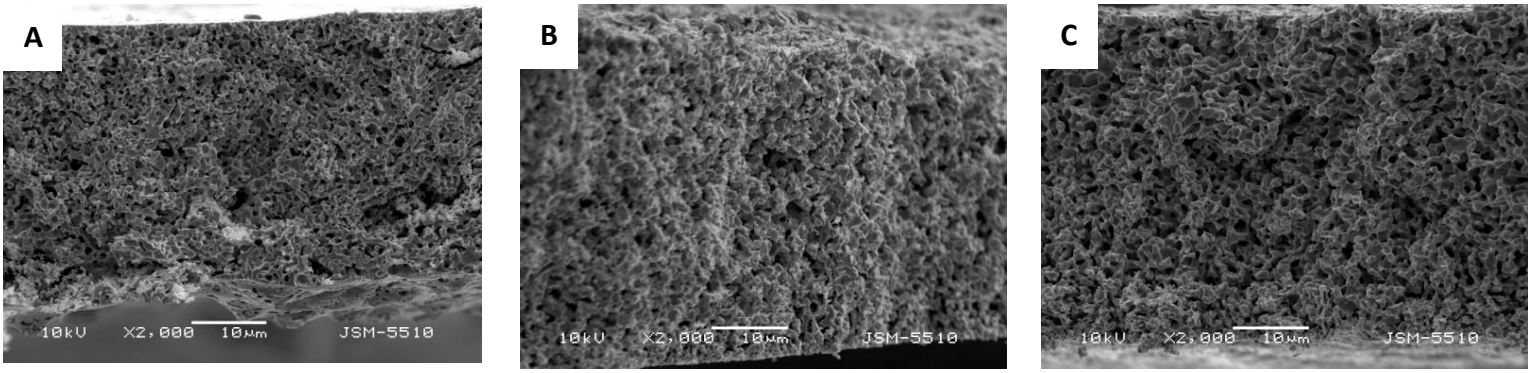

Fig. 35. Cross-sectional SEM of the dealloyed ribbons: $Zn_{70}Sn_5Bi_{25}$ (A), $Zn_{70}Sn_{15}Bi_{15}$ (B) and $Zn_{70}Sn_{25}Bi_5$ (C).

Evidence that under applied conditions of selective dissolution, Zn is the metal that dissolves and Sn and Bi form the porous structure, were also the diffraction curves of the porous materials, Fig. 36. In all three compositions, after dissolution, diffraction peaks of only tin and bismuth are observed, and their intensity is different due to their different content in the initial alloys. The position of the Bi peaks compared to that before dealloying is not changed, whereas the diffraction peaks of Sn after dealloying show a shift to lower angles, corresponding exactly to those of pure Sn. This fact indicates that during the selective dissolution process not only Zn crystallites are dissolved, but also Zn atoms from the Sn(Zn) solid solution are leached.

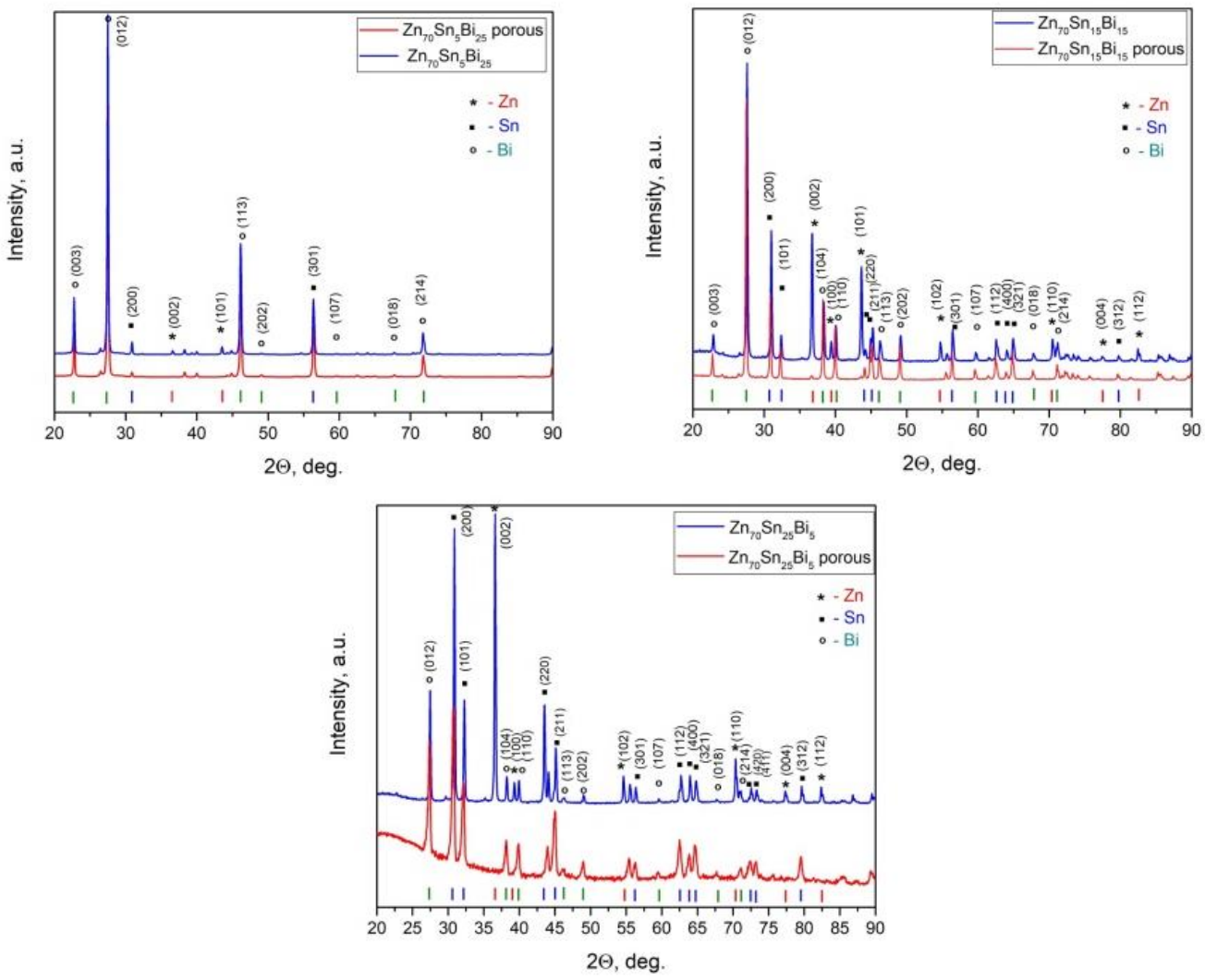

Fig. 36. XRD patterns of $Zn_{70}Sn_5Bi_{25}$, $Zn_{70}Sn_{15}Bi_{15}$ and $Zn_{70}Sn_{25}Bi_5$ ribbons before and after selective dissolution.

Additional TEM/EDS analysis of the three selectively dissolved alloys was performed, Fig. 37, Fig. 38, Fig. 39. The chemical composition corresponds to the ratio of the undissolved metals (Sn and Bi) in the initial alloys. It should be noted that during the samples preparation for the microscopic examination (cutting with an UltraMicrotome), the integrity of the ligaments that form the porous structure is partially lost.

The TEM/EDS results of the porous structures supported the results of the XRD measurements, revealing only Bi and Sn crystals. The distribution of the elements is summarized in Table 3.

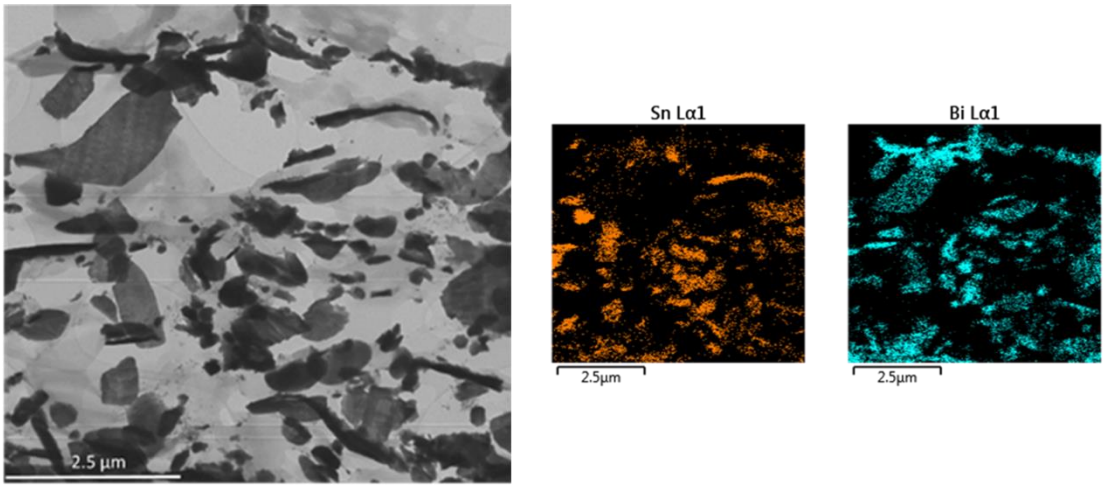

Fig. 37. STEM and EDS of $Zn_{70}Sn_5Bi_{25}$ ribbon after dealloying.

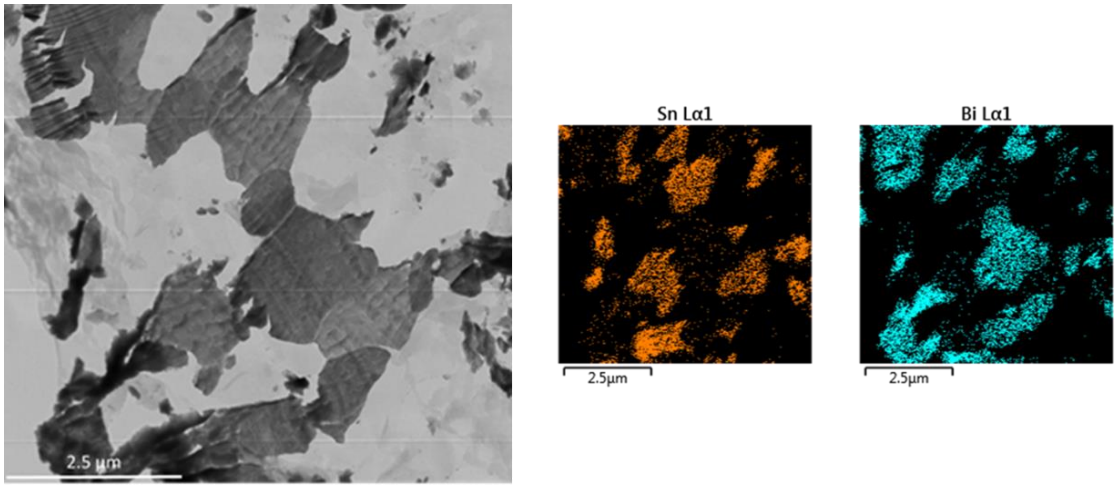

Fig. 38. STEM and EDS of $Zn_{70}Sn_{15}Bi_{15}$ ribbon after dealloying.

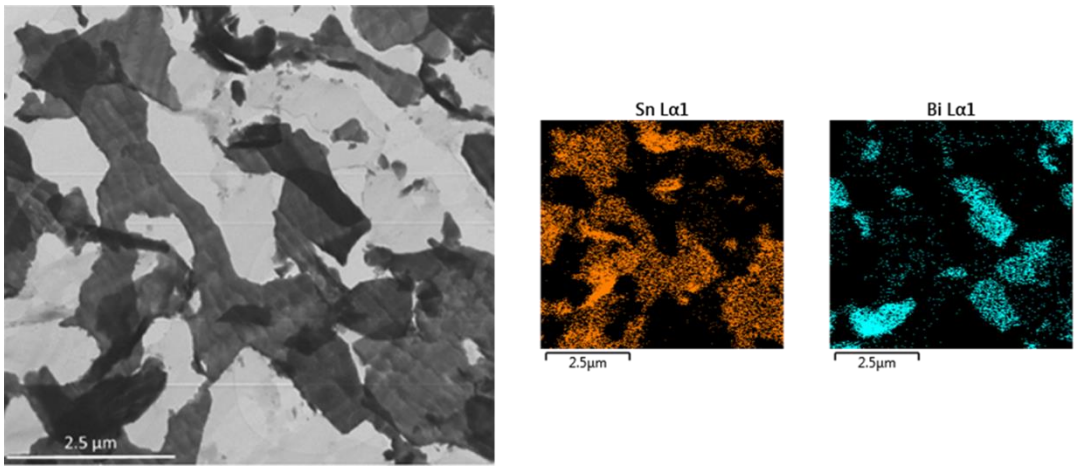

Fig. 39. STEM and EDS of $Zn_{70}Sn_{25}Bi_5$ ribbon after dealloying.

	Zn, at.%	**Sn, at.%**	**Bi, at.%**
$Zn_{70}Sn_5Bi_{25}$ - dealloyed	0,00	30,38	69,62
$Zn_{70}Sn_{15}Bi_{15}$ - dealloyed	0,00	46,39	53,61
$Zn_{70}Sn_{25}Bi_5$ - dealloyed	0,00	68,93	31,07

Table 3. Distribution of the elements from STEM-EDS for the three alloys after selective dissolution.

3. $Cu_{60}Ag_{30}Al_{10}$ alloy

Following the objectives of the thesis, the ternary $Cu_{60}Ag_{30}Al_{10}$ alloy, selected with a suitable composition to form a porous structure with application in ionic batteries, was also investigated.

3.1. Synthesis and microstructural characterization

In order to prepare a porous negative electrode for lithium-ion batteries, alloy with a composition $Cu_{60}Ag_{30}Al_{10}$ obtained by rapid quenching at a rotation speed of the quenching disc of 2000 rpm, was also investigated. The thickness of the ribbon is about 50 μm. The mictostructure of the alloy before and after selective dissolution was studied with X-ray diffractometer Bruker D8 Advance with CuKα radiation and with transmission electron microscope - JEOL JEM 2100, 200 kV. The electrochemical experiments were performed in a three-electrode cell with PARSTAT 2273 potentiostat-galvanostat, the morphology and elements distribution were investigated with scanning electron microscopes - SEM JEOL 5510 and Nova NanoSEM. The chemical composition after sulphur deposition was investigated by energy-dispersive spectroscopy - EDX/JEOL JEM 2100. Coin half-cells (type CR2032) were assembled in an Ar-filled glove box using Celgard tape as a separator, Li foil as a counter electrode and 1 M $LiPF_6$ in a mixture of ethylene carbonate (EC) and dimethyl carbonate (DMC) as electrolyte. The electrochemical characterization were carried out at various current rates using a Bio Logic VNP3B-5 workstation.

The as-prepared melt-spun $Cu_{60}Ag_{30}Al_{10}$ alloy shows a two-phase microstructure, consisting of Ag(Al) and Cu(Al) solid solutions, Fig. 40. The most intensive diffraction peaks of Cu and Ag are well expressed, as their position is slightly shifted due to the partial substitution of Cu and Ag atoms from their face centered cubic crystal lattices with Al atoms. Separate aluminium phases cannot be detected on the X-ray diffraction pattern.

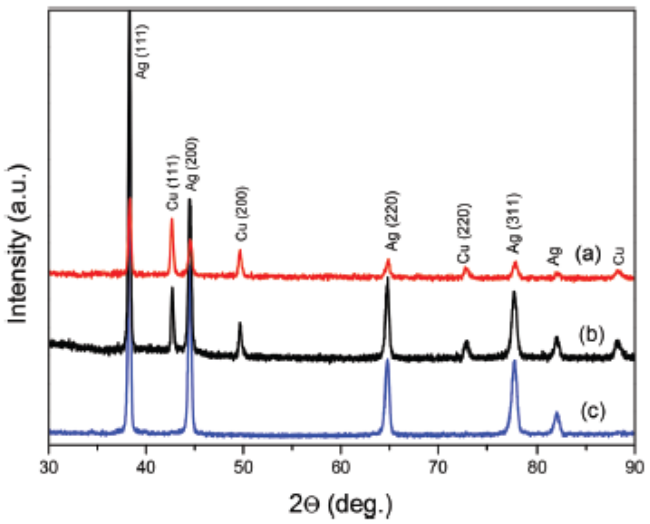

Fig. 40. The XRD patterns of the as-quenched $Cu_{60}Ag_{30}Al_{10}$ alloy (a), and after different times of selective dissolution of the $Cu_{60}Ag_{30}Al_{10}$ alloy in 0,1 M $HClO_4$: 30 min (b) and 120 min (c).

3.2. Formation of porous structure by selective electrochemical dissolution of the initial alloy

Potentiodynamic polatization experiments were performed at a scan rate of 1 mV/s in order to determine the potential for selective dissolution of copper and aluminium from $Cu_{60}Ag_{30}Al_{10}$ alloy, Fig. 41. After the corrosion potential, which is at about 0 V, the current rises rapidly and reaches a maximum, after which there is a slight drop corresponding to the passive region of the alloy. After the passive region, a constant increase in the current is observed due to the corrosion processes, which take place.

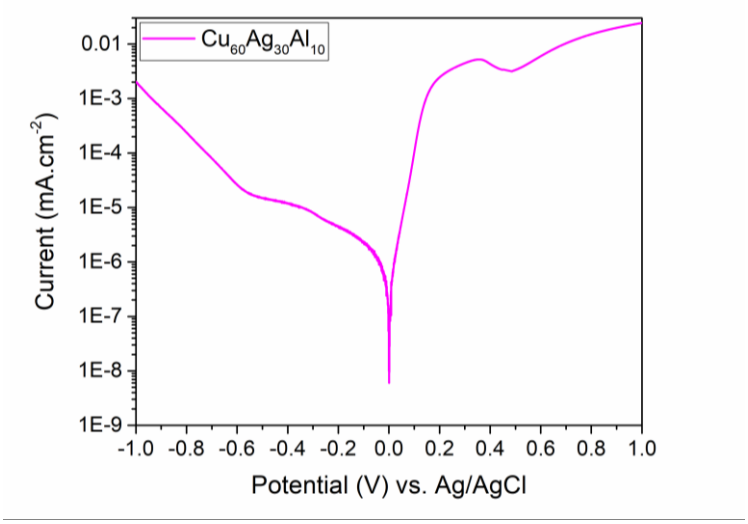

Fig. 41. Potentiodynamic polarization curve of $Cu_{60}Ag_{30}Al_{10}$ alloy in 0.1 M $HClO_4$ water solution.

The chosen potential for the selective dissolution was +150 mV vs. Ag/AgCl, which is just before the passive region of the alloy. The potentiostatic experiments were carried out in 0.1 M $HClO_4$ aqueous solution for 7200 sec, Fig. 42. At the beginning, for a short time, the current increases rapidly and then gradually decreases without significant changes. Depending on the dissolution time, the alloy becomes richer in Ag up to about 75 at.% and at the same time, Cu content shows a noticeable decrease. Nearly complete extraction of Cu is achieved after 120 min of potentiostatic treatment, confirmed by the SEM-EDS analysis and the XRD shown above.

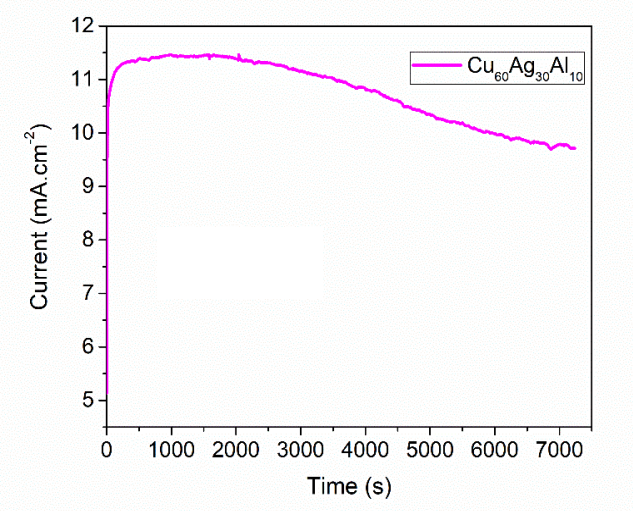

Fig. 42. Potentiostatic curve of $Cu_{60}Ag_{30}Al_{10}$ in 0.1 M $HClO_4$ at 150 mV vs. Ag/AgCl.

To investigate the morphology of the alloy after potentiostatic experiments, the electrodes were analyzed with scanning electron microscope. The SEM micrographs reveal the resulting 3-D porous structure with a well-defined and homogeneous porosity over the whole ribbon surface, Fig. 43. The ligament sizes varies between 100 nm and 200 nm and the sizes of the pores and channels are in the range from 100 nm to 2000 nm.

The specific surface area (S_{BET}) of the dealloyed ribbon was determined – S_{BET} = ~ 2 m^2/g, and also the total pore volume - V_t = 0.007 cm^3/g, and the average pore diameter - D_{av} = 15 nm. The mismatch between the dominant pore size observed by SEM and the one determined by nitrogen adsorption should be noted. This discrepancy could be explained by the presence of a large number of very small pores, which could not be evidenced by the SEM analysis.

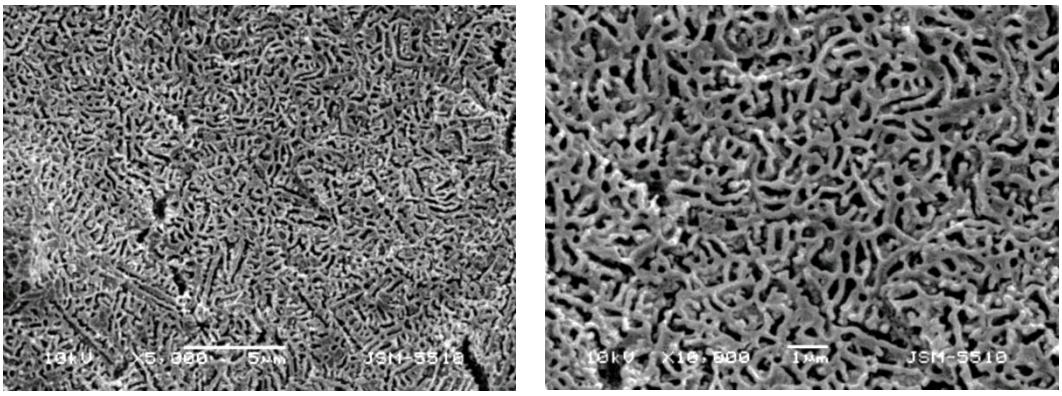

Fig. 43. SEM micrographs of the selectively dissolved $Cu_{60}Ag_{30}Al_{10}$ ribbon.

3.3. Deposition of active material

The obtained porous structure was used as a mechanically stable and conductive scaffold on which an active material was directly deposited by two methods – from a solution and by a direct drop-casting technique. The resulting material was tested as an electrode for ion batteries in the absence of binders and carbon additives.

When sulfur is deposited from a solution, after the selective dissolution the electrode is washed with ethanol, placed in an ultrasonic bath and directly immersed in an 0,01 M Na_2S aqueous solution for 2 minutes. A thickening of the ligaments from sulfur crystals over the entire ribbon surface is observed, Fig. 44.

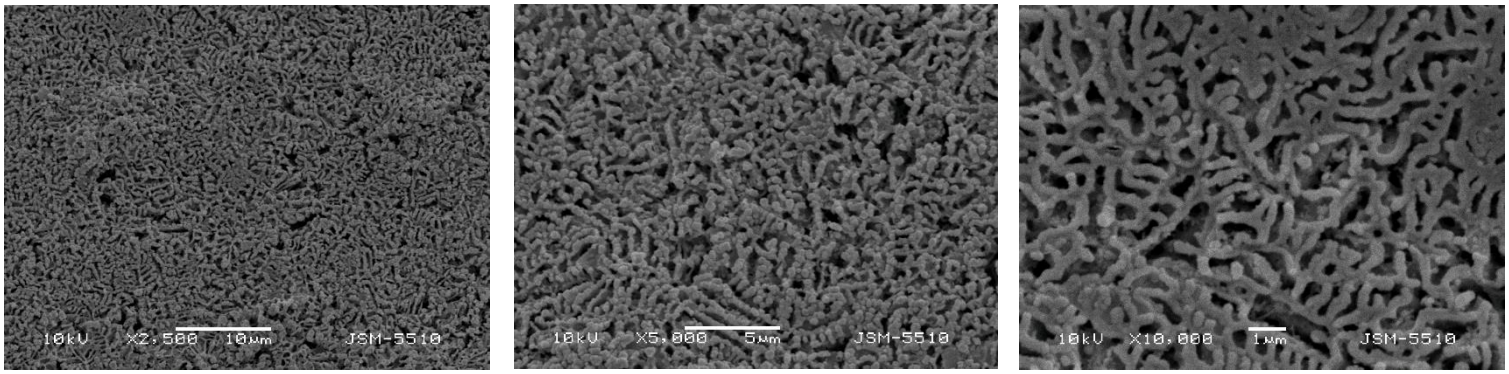

Fig. 44. SEM micrographs of the selectively dissolved $Cu_{60}Ag_{30}Al_{10}$ ribbon after sulfur deposition in 0,01 M Na_2S.

Transmission electron microscopy (TEM) was used to study the changes that occurred in the initial alloy composition as a result of the selective electrochemical dissolution and the sulfur deposition, as well as the elements distribution. Samples were prepared by being fixed in a three-component epoxy resin and cut with an UltraMicrotome with ~ 20 nm slice thickness

The high resolution electron micrographs also confirm the sulfur deposition. The orientation of the formed Ag_2S nanocrystals is along [200] direction, which corresponds to an interplanar distance 0,317 nm, Fig. 45.

.

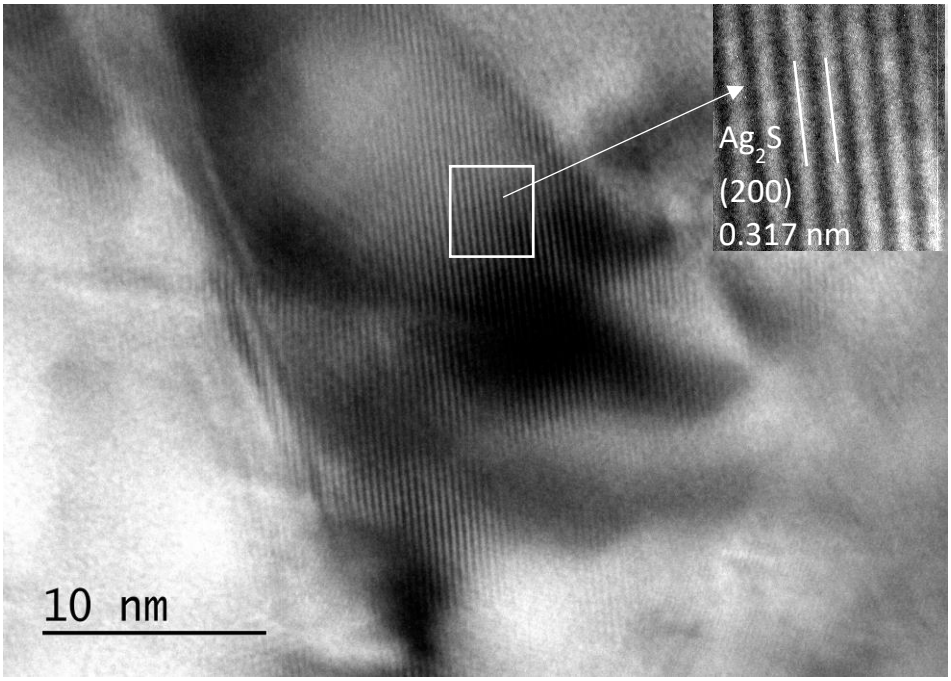

Fig. 45. HRTEM after selective dissolution and sulfur deposition at 600 000 magnification.

The elemental analysis shows almost complete dissolution of Cu и Al from the alloy and the formation of a well-defined porous structure based on Ag. From the colour images, it is evident that the remaining elements, including sulfur, are homogeneously distributed in the silver matrix. The content of the individual elements in atomic % is: Ag – 93.19 at. %; Cu – 3.64 at. %; Al – 1.62 at. % и S – 1.55 at.%, Fig. 46.

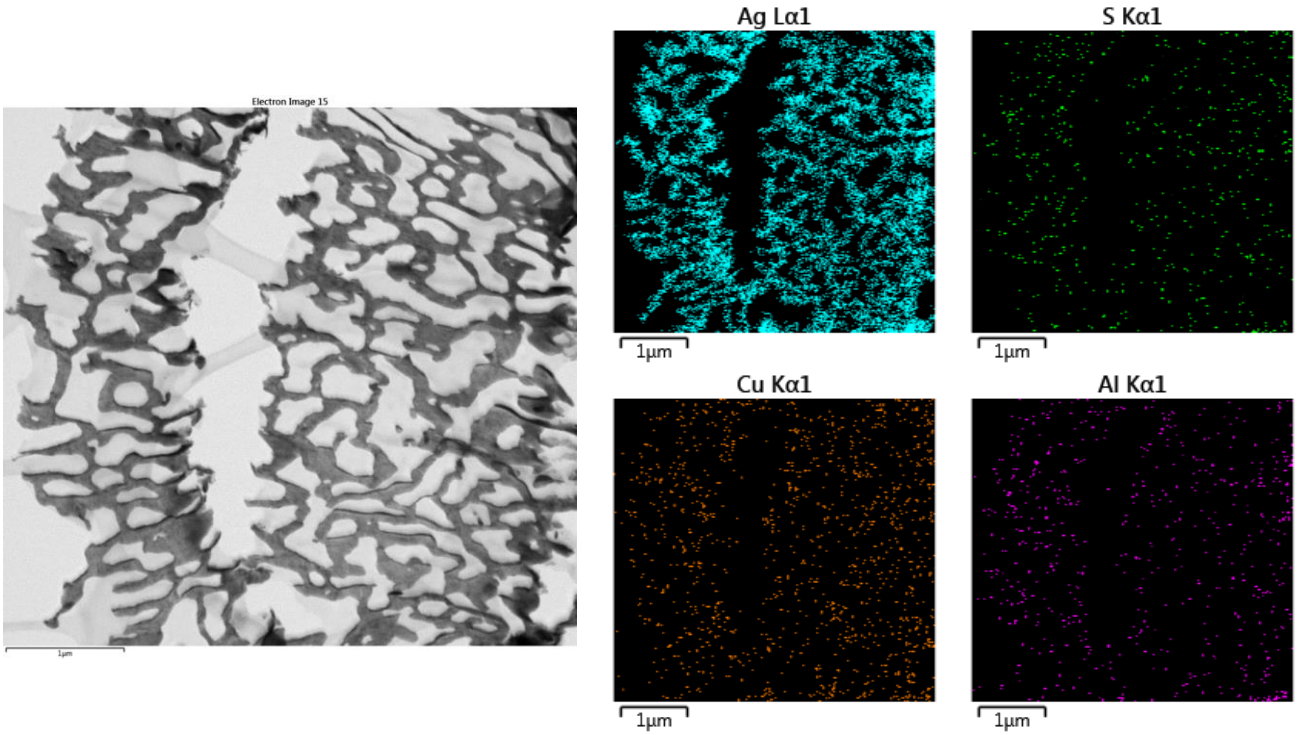

Fig. 46. STEM and EDS of the selectively dissolved $Cu_{60}Ag_{30}Al_{10}$ alloy after sulfur deposition.

When the second approach for deposition of an active material is applied, the porous scaffolds were vacuum infiltrated with sulfur dissolved in toluene. Controlled volumes from 20 to 40 µL of the ink were drop-cast on the porous ribbons in several steps. After each step, the electrodes were exposed to a low vacuum in order to ensure deep ink penetration in the pores. The as-treated electrodes were annealed at 200 °C under Ar gas for 10 min. The active weight of reacted sulfur is ~ 0,25 – 0,3 mg cm^{-2}.

The XRD patterns confirm the presence of the expected monoclinic α-Ag_2S phase, accompanied by the tetragonal Ag_3CuS_2 and orthorhombic $(Ag,Cu)_2S$ intermetallic phases, Fig. 47.

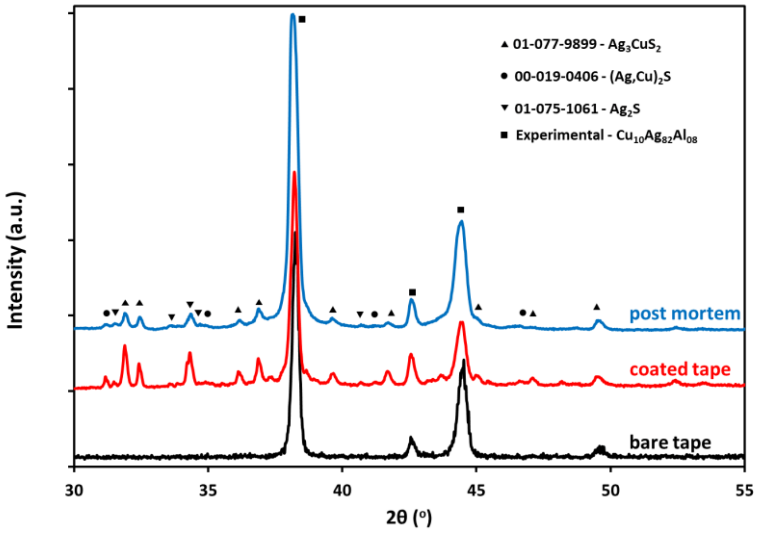

Fig. 47. Comparison of the XRD patterns of dealloyed non-coated substrate and coated electrode, as well as after work in Li-ion cell.

From the SEM/EDS analysis after sulfur infiltration, three different morphologically distinctive areas are marked, Fig. 48 (a). Region **A** represents a submicron (~ 250 nm) thick sulfur-rich layer at the top surface of the ribbon. Region **B** clearly delineates the dealloyed part of the tape with an average composition of $Cu_{10}Ag_{82}Al_8$. Region **C** corresponds to the original dense bottom part of the $Cu_{60}Ag_{30}Al_{10}$ master alloy. The accumulation of sulfur forming a porous top membrane layer is illustrated by the elemental mapping, Fig. 48 (b), with contents of S, Cu and Ag in regions **A** and **B** summarized in Fig. 48 (c). The distribution of sulfur within the porous structure appears to be uniform, without any large segregations, suggesting the good wetting of the substate skeleton by a toluene-based ink.

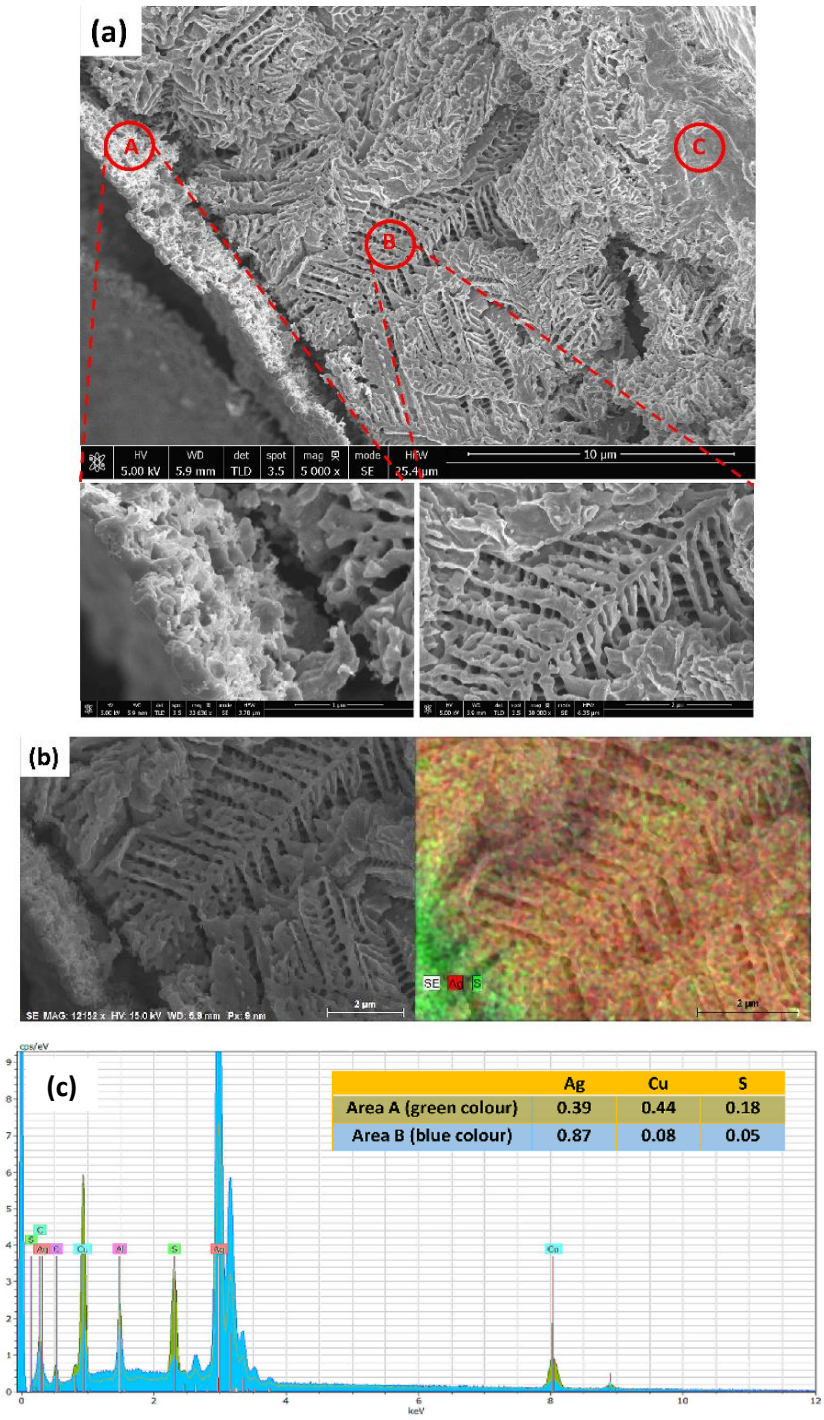

Fig. 48. Cross-sectional SEM images (a) and EDS Ag and S maps (b) of the infiltrated and thermally treated electrodes; (c) EDS spectrum of areas **A** and **B** shown in (a) and the relevant average composition ratios.

3.4. Application of the porous metal structure as a negative electrode component in an ion battery

The results shown are for the electrode obtained by the second approach for deposition of active material. In the initial electrochemical charge/discharge test at a low current rate of 0,1 A g^{-1}, calculated vs. the weight of incorporated sulfur, the discharge process was very slow plateauing at ~ 1,8 – 1,9 V due to the kinetic barrier presented by the sulfur-rich membrane. A specific discharge capacity limit was set at 600 mAh g^{-1} in order to introduce a practical experimental time frame. Fig 49 shows that while the specific charge capacity was observed to increase steadily with each consecutive cycle, the end potential decreased from 1,95 V for cycle one to 1,7 V for cycle ten.

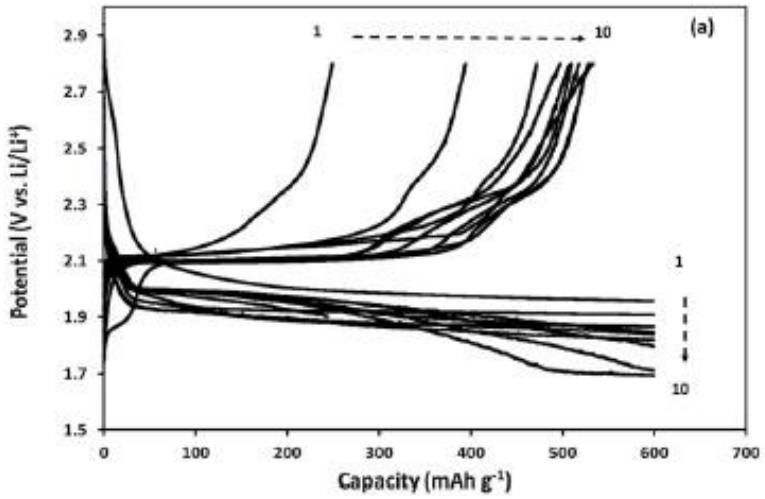

Fig. 49. Potential vs. capacity plots for the first 10 cycles of the Ag_2S-Cu_xS electrode at 0,1 A g^{-1} current rate.

Considering the observed dynamics of the specific charge capacities, the end-potentials and the chemical composition of the layer, we speculate that at 0,1 A g^{-1} current rate, this behaviour accounts for reaction where the sulfur in the layer gradually solvates due to the formation of long chain polysulphides Li_2S_n ($6 \leq n \leq 8$) at a potential of ~ 1.9 V [224, 225].

In the initial several cycles, two reduction plateaus are observed: [217]

- First, an oblique plateau at ~ 2.1-2.2 V where polysulphides with n ~ 6-8 are generated.

$$S_8^0 + 4e^- = 2S_4^{2-}$$

- Second, an apparent plateau for n < 4 at ~ 1.9-2.0 V.

$$S_4^{2-} + 4e^- = 2S^{2-} + S_2^{2-}$$

The low capacity of the first discharge suggests that it does not lead to transformation of polysulphides into elemental sulfur, thus illustrating slow dissolution of the layer. The capacity evolution of the following charges reflects the establishment of the shuttle mechanism where lower-order polysulphides formed at the lithium electrode diffuse back to generate higher forms of polysulphides. The additional sloping plateau appearing at cycle 10 accounts for the Li storage in the Ag_2S-Cu_xS electrode, driven by the displacement lithiation/delithiation reaction.

A summary of the charge/discharge test at a higher rate of 0,4 A g^{-1} is presented in Fig. 50, where we observe in the potential window of 2,8 – 0,15 V the first discharge specific capacity exceeded 1200 mAh g^{-1}, suggesting the partial removal of the membrane kinetic barrier. It is noted that the low initial coulombic efficiency of ~ 75% was due to the formation of SEI layer. The solvation of the residual unreacted sulfur led to a rapid decrease in the specific capacity over the first two cycles. Further cycling resulted in multi plateau shaped charge/discharge curves within the potential window 2,8 – 0,15 V and a gradual decrease in the specific capacity reaching a stable value of 230 mAh g^{-1} after 15 cycles, Fig. 50 (inset).

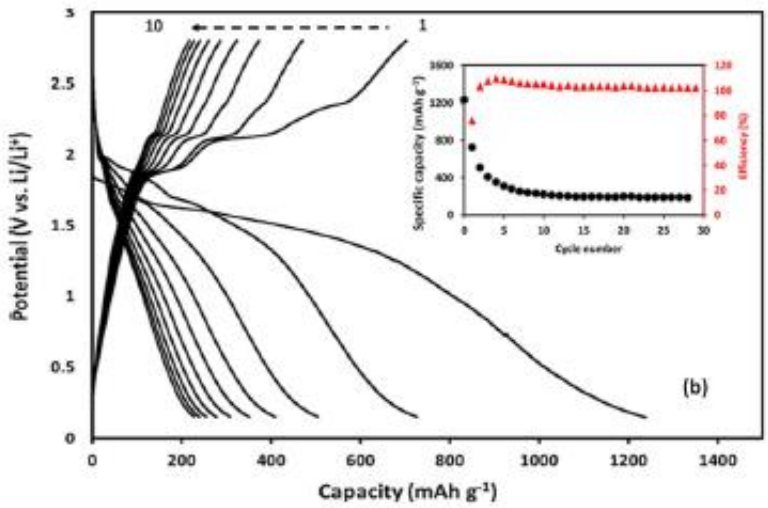

Fig. 50. Potential vs. capacity plots for the first 10 cycles of the Ag_2S-Cu_xS electrode at 0,4 A g^{-1} current rate (the inset shows the evolution of the capacity and efficiency for the first 30 cycles).

This behaviour suggested that the initial rapid capacity decrease was due to the irreversible formation of SEI layer and the solvation of polysulphides, followed by stable cycling associated with the Ag_2S-Cu_xS displacement reaction.

In comparison, the nanocomposite Ag_2S/C electrodes reported by Hwa et al [217], tested in a wider voltage range of 0,0 - 2,5 V exhibited a higher capacity of 430 mAh g^{-1} after 100 cycles accumulated by a combination of "displacement" and "alloying/dealloying" reactions as shown in Fig. 51.

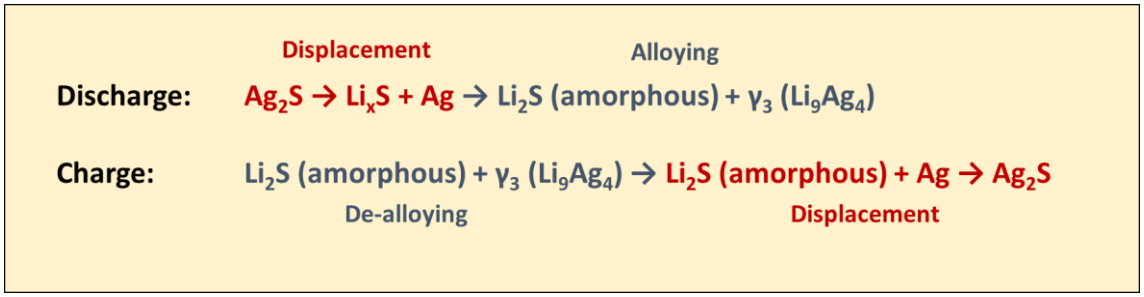

Fig. 51. Combination of reactions involved in a charge/discharge cycles of the Ag_2S electrode in the 2,8 – 0,0 V potential window.

The measured capacity of 230 mAh g^{-1} slightly exceeds the theoretical capacity for Ag_2S (217 mAh g^{-1}), which suggests that in the present work, one has to account for the capacity contribution of the Cu_xS component, whose theoretical specific capacity is higher - ~ 560 mAh g^{-1}. Debart. et al [215] analysed in detail the charge/discharge reaction mechanism related to the Cu_xS electrode. They concluded that the reacting path includes an initial formation of polymorphic $Cu_{2-x}S$ intermediary phase, which transformed further to Cu + Li_2S, as shown:

$$CuS + e^- + Li^+ \leftrightarrow 1/2\ Cu_2S + 1/2\ Li_2S$$
$$½\ Cu_2S + e^- + Li^+ \leftrightarrow 1/2\ Li_2S + Cu.$$

The results in Fig. 52 supports this assumption. There are severeal peaks associated with a multistep reversible reaction mechanism of the $(Ag_x,Cu_y)S_z$ intermetallic phases with Li^+ in the potential window from 1,3 V to 0,7 V during discharging and from 2,4 to 2,0 V during charging. During the first cycle, three reduction peaks located at 1.22, 0.95 and 0.85 V are resolved indicating the multistep reduction process. The oxidation peaks observed at around 2.39, 2.33 and 2.23 V are ascribed to the corresponding delithiation reactions. In the second cycle, the position of the peaks shifts to the left. Such a migration can be attributed to the overpotential caused by the resistance change resulting from the dissolution of the sulfur-rich layer. The potential area above 2.0 V is covered by a broad hump obscuring the peaks commonly associated with the conversion of sulfur to high-order polysulphides. The broad peak that resolved at ~ 1,4 V could be assigned to the formation of an SEI layer.

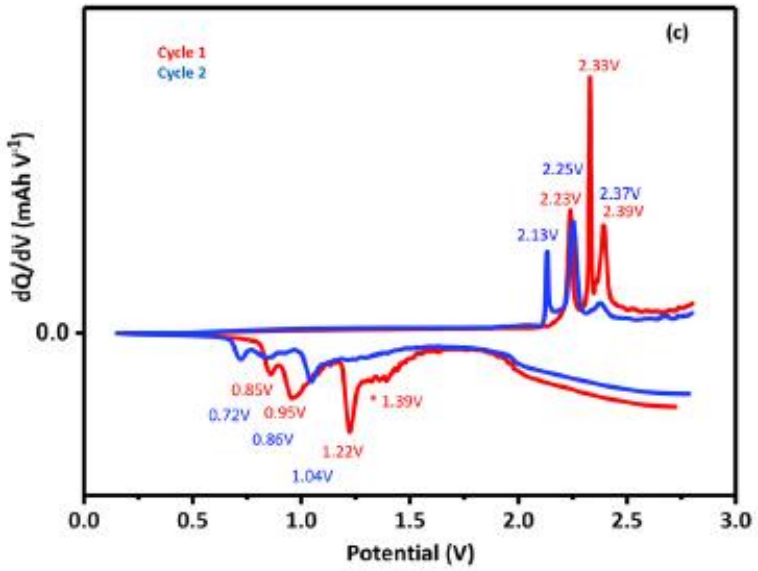

Fig. 52. Differential capacity plot of the Ag_2S-Cu_xS electrode for the first two cycles at 0,4 A g^{-1} current rate.

The Ag_2S-Cu_xS electrode was subjected to long-term cycling and the data summary is shown in Fig. 53. After testing at 1 A g^{-1} and 2 A g^{-1} current rates, the cell was rested for 6 months and re-tested at 1 A g^{-1} current rate. Stable cycling performance of the Ag_2S-Cu_xS electrode were recorded for over 1200 cycles. After 250 cycles at 1 A g^{-1} current rate, the average specific capacity of ~ 150 mAh g^{-1} with a retention of ~ 98%, and after 450 cycles the average specific capacity was ~ 200 mAh g^{-1} with a retention of ~ 85%. After 500 cycles at 2 A g^{-1} current rate – average specific capacity of ~ 120 mAh g^{-1} with a retention of ~ 97%.

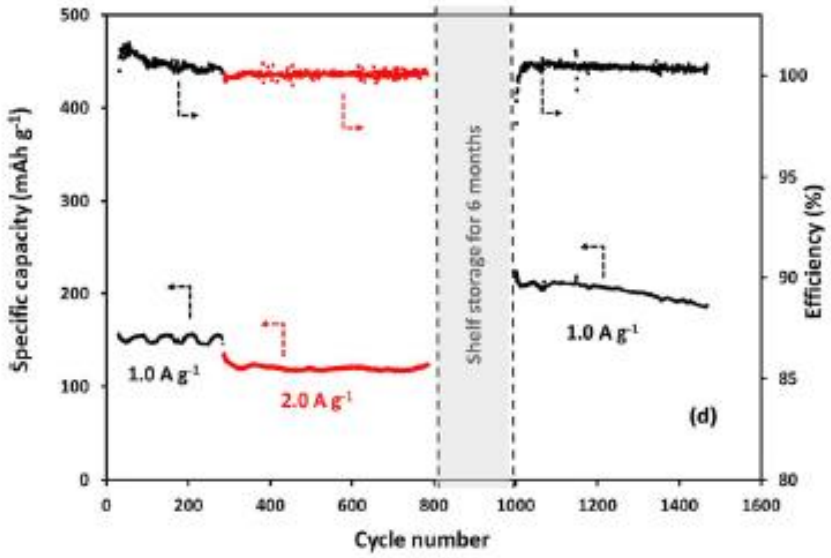

Fig. 53. Long-term cycling performances at current rates of 1 A g^{-1} and 2 A g^{-1}.

The observed stable cycling behaviour and rate performances could be attributed to the nature of the "displacement" reaction, which is promoted by the high mobility of Ag, Cu and Li ions in the metal sulphide electrode. The diffusion coefficients of Ag^+ and Li^+ ions in the Ag_2S phase measured and calculated by different authors are summarized in Table 4. During the reduction phase Ag and Cu diffuse to the surface and form randomly directed dendrites encompassing the Li_2S matrix [215]. Reversibly, during the charge state, Li is extracted and (Ag, Cu) sulphide components are re-oxidised to metal sulfides.

We speculate that the stable charge/discharge cycling at higher rates of 1 A g^{-1} and 2 A g^{-1} observed in this work is a result of the described process, which largely avoids the pulverization of the electrode and suppresses the dissolution of polysulphide intermediates (Li_2S_n) ($4 \leq n \leq 8$).

Ion	Lattice	Diffusion coefficient, (cm^2 s^{-1})	Activation energy, (eV)	Method
Ag^+	Ag_2S	7,34 x 10^{-10}	0.4	Calculated [226]
	Ag_2S	1,97 x 10^{-7}	-	Experimental [227]
Li^+	Ag_2S	2,34 x 10^{-11}	0.52	Calculated [228]
	Ag_2S	~ 10^{-8}	-	Experimental [216]

Table 4. Summary of published data on the diffusion coefficients and activation energies of Ag and Li in Ag_2S matrix.

After a ~ 6 months shelf storage, the re-tested electrode exhibited a noticeable jump in the specific capacity, Fig. 53. This phenomenon could be explained by the fact that some slow erosion of the electrode wall at higher current rates nevertheless took place, resulting in an extension of the active surface area by the formation of a nanostructured top layer. During the long shelf storage, this part of the electrode wall would react with the dissolved polysulphides forming a new portion of the active metal sulfire coating. The as-created enhanced active surface area would contribute to the observed increase in the specific capacity.

Post-mortem SEM/EDS analyses were performed after the completion of the cycling tests. It is apparent that after more than 1000 cycles, the electrode preserved its porous structure and mechanical integrity. A ligament wall thickness of ~80 – 100 nm was detected, confirming the absence of substantial pulverization during the electrode operation, Fig. 54 (A). The EDS mapping also confirms the uniform distribution of sulfur in the Ag matrix, Fig. 54 (B).

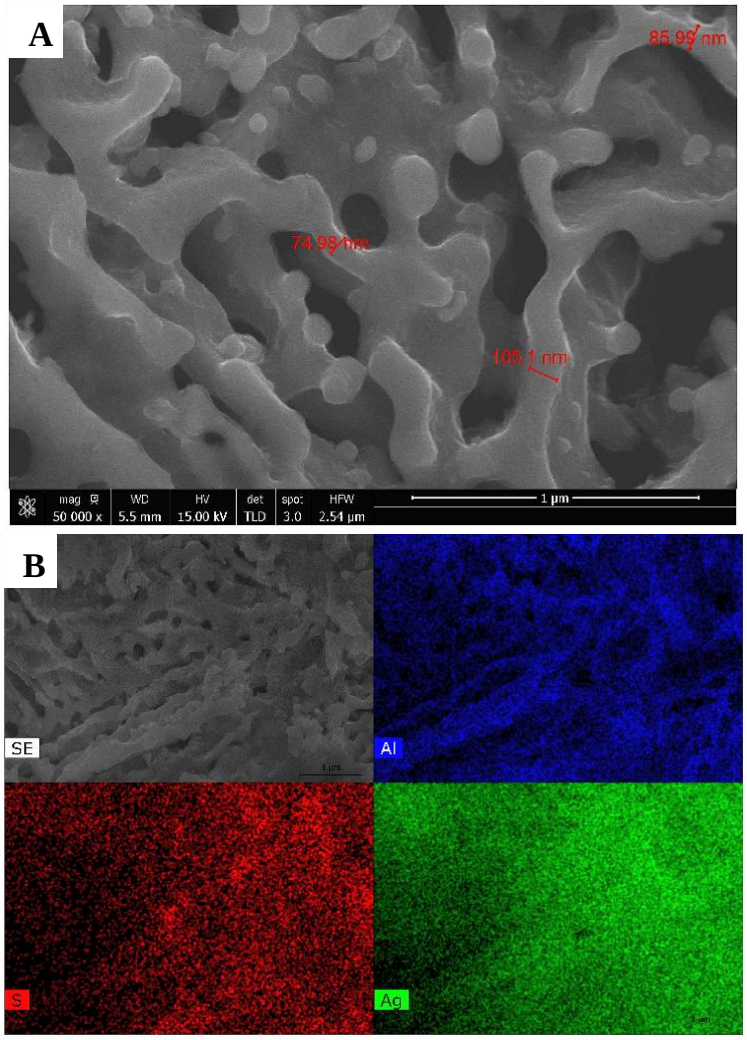

Fig. 54. Post-mortem SEM/EDS analyses: (A) top view of the electrode and (B) cross-sectional EDS mapping of Ag, S and Al distribution.

The long-term cycling results suggest an important application of the Ag_2S-Cu_xS nanocomposite as a polysulphide dissolution inhibitor via strong interactions with the polysulphides during the redox processes. It effectively adsorbs the polysulphides thus reducing the shuttling effect and improving the long-time battery performance. In contrast to other adsorbing additives such as Ti_4O_7 and MnO_2 [229,230], the Ag_2S-Cu_xS nanocomposite contributes additional capacity in the voltage range above 1.5 V. Additionally, the proposed electrode produces a conductive metal in the reversible reaction thus improving the electronic conductivity of the electrode.

IV. Conclusions

From the study on series of two- and three-component alloys based on ***Zn-Sn and Zn-Sn-Bi***, the following conclusions can be drawn:

1. Alloys with composition $Zn_{70}Sn_{30}$, $Zn_{70}Sn_{25}Bi_5$, $Zn_{70}Sn_{15}Bi_{15}$ and $Zn_{70}Sn_5Bi_{25}$ were obtained by rapid quenching. Also, an alloy with composition $Zn_{70}Sn_{30}$ was obtained by normal cooling and casting on a ceramic surface. In dependence on the preparation method, a difference in the microstructure of the alloys was observed: the melt-spun ribbons are characterized by smaller crystallite size and a more homogeneous phase distribution compared to the conventionally cooled alloy.

2. By applying a combination of electrochemical analyses, the appropriate conditions (electrode potential, type and concentration of the electrolyte, dissolution time) for the selective electrochemical dissolution of the less noble element from the alloys were determined.

3. A dependence between the initial composition of the alloys and the morphology, size of the pores and ligaments of the resulting porous structure was established.

4. The porous $Zn_{70}Sn_{30}$ alloy was tested as an electrode for Li/Na-ion batteries. The initial discharge capacity in the lithium cell was found to be about 440 mAh/g, and in the sodium cell – 250 mAh/g. Better charge/discharge cycling stability of the porous electrode in the Na-ion cell was determined.

From the study on $\boldsymbol{Cu_{60}Ag_{30}Al_{10}}$ alloy, the following conclusions can be drawn:

1. A microcrystalline $Cu_{60}Ag_{30}Al_{10}$ alloy was obtained by rapid quenching.

2. The appropriate conditions for the selective electrochemical dissolution of Cu and Al from the alloy were selected. As a result, homogeneous porosity across the whole ribbon thickness with ligaments sizes in the range of 100 to 200 nm and pore and channel sizes in the range of 100 to2000 nm was obtained.

3. The porous structure was used as a mechanically stable and conductive scaffold, on which active material sulfur was directly deposited. For this purpose, two approaches we applied – from a solution and by a direct drop-casting technique.

4. After sulfur deposition, the electrodes were electrochemically tested in a half-cell configurations vs. Li/Li^+. A reversible capacity of ~ 230 mAh/g was measured at a current rate of 0.4 μA cm^{-2}.

5. The electrode performance was shown to be stable over 1000 cycles at a 1 and 2 A g^{-1} current rates. This longevity and rate performance were attributed to the displacement reaction of the Ag_2S-Cu_xS active material with Li ions.

Scientific contributions

1. An original methodology for obtaining eutectic type two-component (Zn-Sn) and three-component (Zn-Sn-Bi, Cu-Ag-Al) alloys was applied and as a result, a fine microstructure and homogeneous distribution of the existing crystal phases was achieved.

2. The appropriate conditions (electrode potential, type and concentration of the electrolyte, dissolution time) for electrochemical selective dissolution of the synthesized alloys were established. As a result, porous structures with pore and ligament sizes in the nanometric range were obtained.

3. The porous structures based on Bi and Sn are shown to be suitable negative electrodes in Li/Na ion batteries, operating on the “alloying” principle with Li/Na. The measured discharge capacities are promising and motivate the expansion of research in the direction of optimizing the microstructure of the alloys, in order to achieve high and stable cycling capacity of the battery.

4. An original methodology was applied to study the capacity and stability of lithium-sulphur batteries, where a porous metal structures are used as mechanically stable and conductive scaffolds, on which sulfur was directly deposited.

Scientific publications related to the dissertation

- Vassileva, E., Mihaylov, L., Boyadjieva, T., Koleva, V., Stoyanova, R., & Spassov, T. (2021).

Porous Sn obtained by selective electrochemical dissolution of melt-spun $Zn_{70}Sn_{30}$ alloys with lithium and sodium storage properties.

Journal of Alloys and Compounds, *877*, 160319, **Q1**.

- Tomov, R. I., Mihaylov, L., Bird, L. R., Vassileva, E., Kumar, R. V., Chhowalla, M., & Spassov, T. (2022).

On the performance of a hierarchically porous Ag_2S–Cu_xS electrode in Li-ion batteries.

Dalton Transactions, *51*(47), 18045-18053, **Q1**.

- Vassileva, E., Mihaylov, L., Spassova, M., & Spassov, T. (2023).

Porous metallic structures by de-alloying microcrystalline melt-spun ternary $Zn_{70}(Sn, Bi)_{30}$.

Journal of Porous Materials, *30*(2), 485-492, **Q2**

The results of the dissertation work have been presented at the following scientific forums

- Scientific conference Inframat 2021, Pravets 08-10.09.2021, *Report*

E.Vassileva, L. Mihaylov, T. Boyadjieva, V. Koleva, R. Stoyanova, T.Spassov,
"Porous Sn obtained by selective electrochemical dissolution of melt-spun $Zn_{70}Sn_{30}$ alloys with lithium and sodium storage properties"

- National Student Conference in Pharmaceutical and Chemical Sciences 2022, Faculy of Chemistry and Pharmacy 5-6.10.2022, *Poster*

E.Vassileva, L. Mihaylov, T.Spassov
„Porous Ag obtained by selective electrochemical dissolution"